Vortex formation in narrow ferromagnetic rings

2003 J. Phys.: Condens. Matter 15 R985

(http://iopscience.iop.org/0953-8984/15/21/201)

INSTITUTE OF PHYSICS PUBLISHING JOURNAL OF PHYSICS: CONDENSED MATTER

J. Phys.: Condens. Matter **15** (2003) R985–R1023 PII: S0953-8984(03)33407-1

TOPICAL REVIEW

Vortex formation in narrow ferromagnetic rings

M Kläui, C A F Vaz, L Lopez-Diaz and J A C Bland

Cavendish Laboratory, University of Cambridge, Madingley Road, Cambridge CB3 0HE, UK

Received 1 April 2003
Published 19 May 2003
Online at stacks.iop.org/JPhysCM/15/R985

Abstract

The high-symmetry ring geometry is shown to exhibit a wide range of intriguing magnetostatic and magnetodynamic properties, which we survey in this topical review. We consider first the patterning and deposition techniques, which are used to fabricate ring structures (diameters between 0.1 and 2 μm) and discuss their respective advantages and disadvantages. The results of direct nanoscale imaging of the novel magnetization configurations present in rings with different geometrical parameters (including discs) are discussed. These results give valuable insight into the influence of the magnetic anisotropies governing the magnetic states. The different types of domain walls that arise are compared quantitatively to micromagnetic simulations. The magnetodynamic switching between the different magnetic states is described in detail. In particular we elaborate on the different geometry-dependent magnetic switchings, since the different transitions occurring allow us to determine which energy terms govern the reversal process. We discuss a process by which fast (sub-ns) and controlled switching can be achieved, therefore making rings an attractive geometry for applications, in addition to studying fundamental issues of nanomagnetism.

(Some figures in this article are in colour only in the electronic version)

Contents

1. Introduction

Small magnetic elements have received considerable attention recently, in large measure due to the booming research activity in nanoscience and due to their potential for applications in nanotechnology. These applications include memory elements in high-density storage media or as miniaturized sensor elements [1, 2], while from a more fundamental point of view, the small length scale and low dimensionality lead to new and enhanced properties over bulk materials. This is in particular true when element sizes approach certain characteristic length scales, such as the spin diffusion length, carrier mean free path, or magnetic domain wall width, etc.

In practice, it is challenging to characterize such small magnetic nanostructures, and the need for appropriate measurement methods has led to the development of many novel experimental techniques. Of particular interest is the study of the equilibrium magnetic states and magnetization reversal mechanisms in small elements, which are strongly determined by the interplay of magnetic anisotropies (e.g. magnetocrystalline, interface, etc) with the physical shape of the element. In fact, on the micrometre scale the shape of the element so fundamentally influences the switching behaviour of the magnetization that a large effort has been spent with the purpose of finding the geometries that provide the simplest, fastest, and most reproducible switching mechanism, which are essential prerequisites for device applications [1, 3–7].

To control the magnetic switching precisely, one needs firstly to have a well defined and reproducible remanent state and, secondly, the switching process itself must be simple and reproducible. Different geometries have been studied for this purpose, from simple circular discs [5, 8] to more advanced needle-shape elements [9]. In such topologically simple elements, the aim is to obtain a single-domain state and switching by coherent rotation [10]. However, due to the demagnetizing field induced by dipole interactions, the magnetization direction will always change close to the borders to form edge domains [4, 8]. The magnetic configuration in these elements, therefore, is defined by the shape of the edges and is very sensitive to shape fluctuations and edge roughness. The edge inhomogeneity in the magnetization will dominate the magnetic switching properties, acting as nucleation sites for what is, in general, a complicated nucleation propagation switching process, where the magnetization passes through inhomogeneous intermediate states. The complex switching mechanism can lead to different remanent states depending upon the applied field history and hence influence the switching itself. One possible way to overcome these complications in circular elements is to use the vortex state in which the magnetic flux is closed in the element and where the edge roughness and edge domains play a minor role. The zero stray field in this state will also favour high-density storage. However, the vortex is only stable in discs for diameters

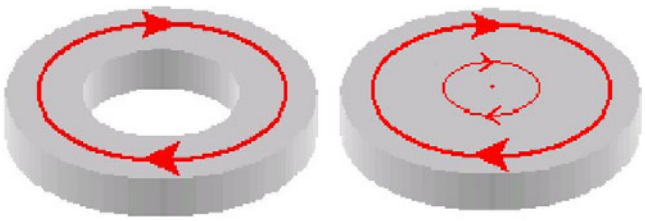

Figure 1. Schematic representations of the vortex state in a ring and a disc.

above some 100 nm [5], depending on the thickness and the material, which limits the density achievable. Moreover, the vortex formation is complex and hard to control [5, 7]. The vortex state can be made more stable if the highly energetic vortex core is removed by using the high-symmetry ring element [11] (figure 1), which has also been proposed for use in magnetic random access memories (MRAM) [1, 12] and as sensors [2, 12]. Apart from the improved stability, the vortex state in ring structures is also completely stray field free, whereas in discs the magnetization in the vortex core is pointing out of the plane of the film, creating a stray field. In addition to potential technological applications, the high-symmetry ring geometry has proven to be valuable for the investigation of fundamental physical questions, such as the pinning and structure of domain walls at notches (constrictions) [13, 14], magnetoresistance effects associated with domain walls [14], and quantum effects such as Aharonov–Bohm oscillations [15]. While in this article we discuss non-interacting isolated rings, earlier work in our group by Hirohata *et al* [16] and work by Welp *et al* [17] has elucidated the properties of ring chains. The related square ring geometry ('picture frame') has also been investigated [18].

This review article is intended to be a report of the current state of the research, bearing in mind that this field remains in constant progress. Unless explicitly stated, we shall present our own work, but we attempt to reference as fully as possible relevant work by other groups working in this very active field. For the inevitable omissions of important work, we can only take this opportunity to apologize. This article is organized as follows. In section 2 we explain the different methods that have been employed to fabricate rings, which include using prepatterned substrates, lift-off, and patterning continuous films into rings. The morphology and magnetism of the thin films used is presented in section 3. Section 4 deals with the magnetic states that occur in rings, in particular the states that are stable at remanence and have been observed with various techniques. Finally, the wide range of switching behaviours in rings is discussed in section 5, including dynamic switching using field pulses.

2. Fabrication

The fabrication of small patterned elements can be achieved in several ways:

(i) by patterning the continuous film by lithography and milling;
(ii) by directly depositing the magnetic metallic layer onto a prepatterned substrate; or
(iii) by deposition of the magnetic film structure onto a substrate where the photoresist pattern has been developed and where the structure is retrieved after a final lift-off step.

All these methods have advantages and disadvantages. The first method is the most conventional, and allows the patterning of any available magnetic film (limited to the capabilities of the lithographic process in being able to process such film and/or material). The disadvantage is that the lithographic process is strongly dependent on the particular materials employed in the structure and also on the particular structural parameters of the film (such

as layer thicknesses). It involves, usually, the determination of the best etching process (dry or wet etching, etching agents, and etching processes for the different materials involved in the film structure). In particular, the patterning of epitaxial structures with a thick buffer layer (between the substrate and the magnetic film) is very difficult (e.g., Ni/Cu(001)/Si(001) or Co/Cu(001)/Si(001)). Another disadvantage is that the lithographic process is likely to introduce some degree of chemical contamination and structural changes in the magnetic film, thereby introducing changes in the magnetic properties (although this can be controlled to some extent by subjecting a large portion of the continuous film to the same heat/chemical treatment to check for changes in the magnetic properties). The use of prepatterned substrates [3, 19] avoids this problem by depositing the magnetic structure on top of the semiconductor substrate which has been patterned prior to deposition. If the structures have a sufficiently high aspect ratio, they will then be disconnected from the continuous background film. This process is compatible with MBE growth and minimizes the risk of contamination of the ultrahigh-vacuum (UHV) environment. The main disadvantage consists of the presence of a large magnetic background, which makes the magnetic characterization more difficult. The last process mentioned here has the advantage of simplicity and a large versatility in terms of the structures that can be deposited, and the only drawbacks are the limitation in the total thickness that can be deposited (which must be smaller than the photoresist thickness; but this limitation is in fact common to all the above-mentioned patterning processes), and the risk of introducing contaminants into the UHV environment, although we have not noticed any detrimental effects in the magnetic properties of the magnetic films. Although the substrate cannot be annealed, epitaxial growth of fcc Co has been achieved [20]. We will now describe in more detail the last two processes, which we have used for the fabrication of the ring structures used in the studies we present in this paper. There is no definite answer for which fabrication method yields the 'best' rings, as this depends very much on the desired properties and the measurements that are planned to be carried out. Furthermore, judging the quality of the ring structure is again very dependent on the criteria applied (good reproducibility of switching fields, agreement with micromagnetic simulations, etc). We will discuss this issue further when we present the magnetic measurements on the differently fabricated structures.

2.1. Prepatterned substrates

To achieve reproducible switching, the magnetic ring should be as 'perfect' as possible. The first fabrication process used is based on prepatterning of silicon ring structures and subsequent epitaxial growth of a Cu/Co/Cu sandwich film on top of the silicon rings. In this technique the magnetic film is not etched or otherwise damaged after deposition. There are a number of challenges in patterning the ring geometry by electron-beam lithography and reactive ion etching (RIE), and the e-beam lithography and silicon etching processes have to be optimized specifically for making the ring elements.

2.1.1. Electron-beam lithography. Electron-beam lithography is known to have the highest resolution compared with other lithography methods. Using either PMMA resist or chemically amplified resists, sub-50 nm lines and dots have been successfully patterned [21, 22]. The difficulty with rings lies in the delineation of the central hole. It is known that electrons scatter in resist and substrate away from their intended area of exposure, causing the proximity effect. As a consequence, the smaller the central hole the more difficult it is to avoid exposure of the central area. For the ring geometry pattern, the proximity effect becomes more pronounced because the central hole is surrounded by exposed area. Figures 2(a)–(d) show a series of four ring patterns with different sizes of central holes. The rings were exposed using a VB6-HR

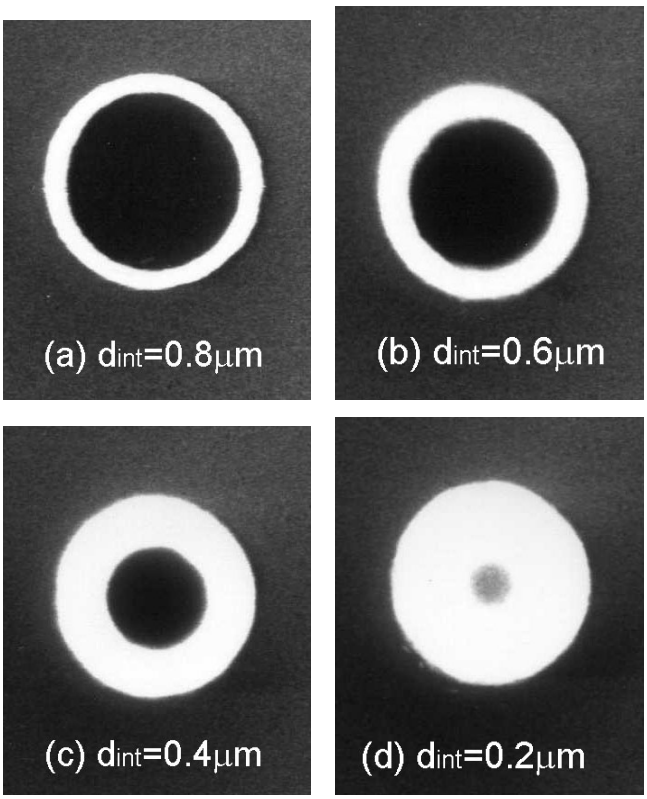

Figure 2. Ring structures with 1 μm outer diameter and different inner diameters (d_{int}).

e-beam lithography system at 100 keV beam energy and the resist is AZPN114 negative tone chemically amplified resist from Clariant. The resist layer thickness is 0.8 μm. The 0.2 μm central hole in figure 2(d) has been partially exposed by electrons from the surrounding exposed area, and therefore could not be fully developed. There are two ways to overcome the electron proximity effect in e-beam lithography. Dedicated proximity correction software, such as CAPROX (from Sigma-C GmbH), has been developed, which can automatically reallocate exposure dose to reduce the electron scattering effect. However, attempts to use CAPROX to correct the proximity effect in sub-micrometre ring patterns were not successful. The software could not fracture the ring pattern, and therefore could not reassign the exposure dose at different parts of the ring. Without the help of proximity correction software, the only option left is to optimize exposure and resist process conditions to minimize the proximity effect. High electron energy and thin-layer resist have been used, and resist development conditions have been optimized. Figures 3(a) and (b) show ring patterns with 200 and 100 nm inner holes, respectively.

2.1.2. Silicon etching. The critical point of the new technology for making magnetic ring elements based on prepatterned substrates is the prepatterning of silicon rings, which then allows for epitaxial growth of magnetic layers on top of the rings. The resist ring structure defined by e-beam lithography has to be transferred to the silicon substrate. Because the magnetic layer is deposited all over the silicon substrate like a blanket, the silicon rings have to be high enough that the magnetic layer on top of the rings is disconnected from the magnetic

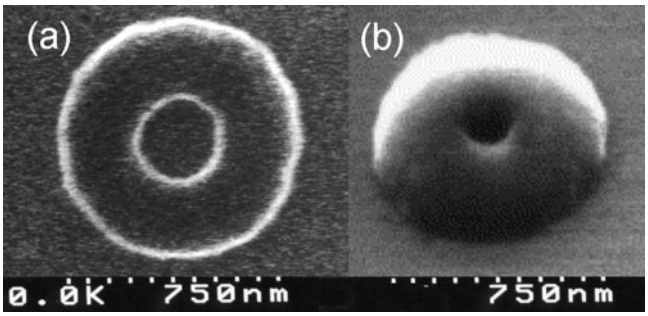

Figure 3. Ring structures of different diameters $d_{\text{int}} = 100$ nm (a) and 200 nm (b) made from thinner (200 nm thickness) resist.

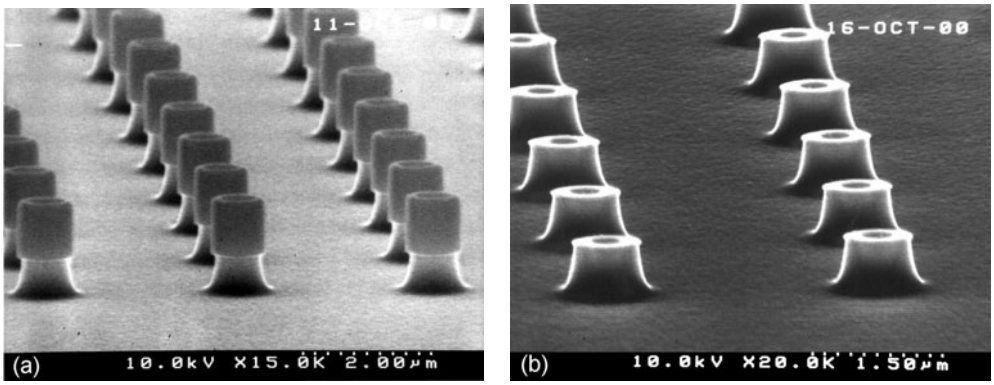

Figure 4. Conventional RIE of silicon rings: (a) an etched ring feature before removal of the resist mask and (b) after removal of the resist mask.

layer in the trenches in between. Conventional RIE of silicon using $SF_6 + O_2$ plasma is not completely anisotropic, so the etched ring structures are not perfectly vertical. Figure 4(a) shows an array of etched rings with the resist masking layer still on top and figure 4(b) shows the rings after removal of the resist. Isotropic etching can be used to vary the ring width by controlling the etching time: figure 5(a) shows an array of silicon rings after 1.5 min of etching and figure 5(b) shows the same rings after an additional 0.5 min of etching. The ring width becomes much narrower with increased etching time. The ideal profile for an etched silicon ring is to have an overhang at the top so that the deposited magnetic film at the top of the rings will be discontinuous with the film at the bottom. With conventional RIE it is extremely difficult to produce such profiles because of the etching profile produced, as shown in figures 4 and 5. There is a new deep silicon etching process which has been widely used for producing microelectromechanical system (MEMS) structures. The deep silicon etching process, called the Bosch process, is based on switching gases from etching to passivation in a short cycle [23]. Etching silicon by the Bosch process always produces a slightly overhanging profile, which is ideal for depositing magnetic rings. The Bosch process, which so far has only been used for etching larger and deeper structures, has been adapted for etching ring structures of sub-micrometre size and depth. By optimizing the gas chopping cycle, it is possible to produce a large array of silicon rings with a near-vertical profile, as shown in figure 6.

After prepatterning of the silicon, a copper template layer and then the single-crystal cobalt layer (34 nm thick) are grown on top of the silicon rings in a molecular-beam epitaxy (MBE)

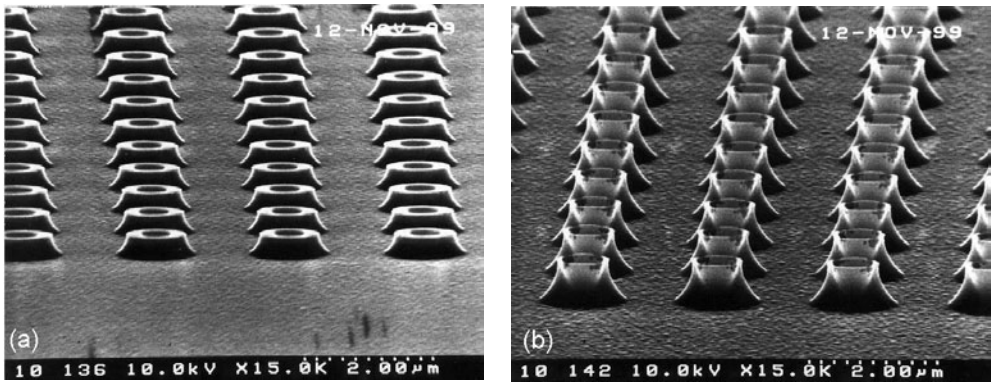

Figure 5. Etched ring features over different lengths of time: (a) 1.5 min and (b) 2 min.

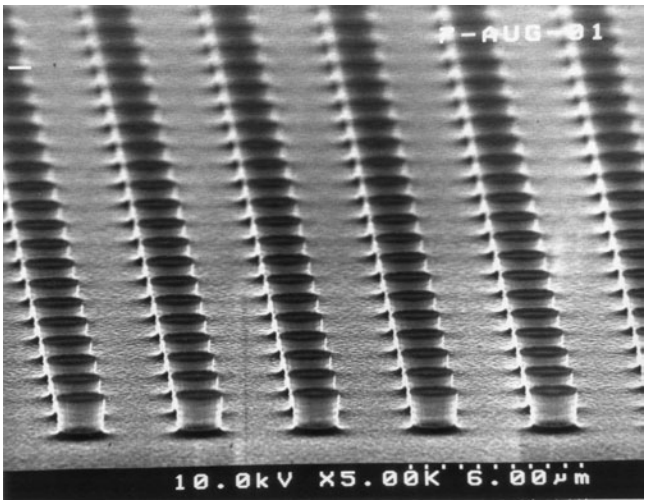

Figure 6. Silicon ring structures etched by the Bosch process.

system (see section 3). The overhanging profile of the etched silicon rings ensures that the magnetic film on top of the rings is disconnected from the substrate floor. They behave like individual magnetic rings even though the film is deposited as a blanket over the whole substrate (see figure 7).

2.1.3. Physical separation between rings and the trenches. A concern with these samples is the magnetic coupling between the desired magnetic structures on the summits and the magnetic material in the trenches. This coupling is mainly dipolar, resulting from the stray field at the edge of the trenches, but direct exchange coupling can also arise if the Co on the summits is physically connected to the Co in the trenches. The rings were obtained by depositing a trilayer Cu/Co/Cu on Si(100). An SEM graph of one of the rings after deposition of the epitaxial layers (100 nm Cu, 34 nm Co, 2 nm Cu) is shown in figure 8. The image reveals that both a significant asymmetry and an edge roughness exist, due to the fast standard etching of the Si. We note that the surface on the top of the ring is flat, which shows that the magnetic rings have thin-film shape. The edge of the metallization in the trenches can be observed on

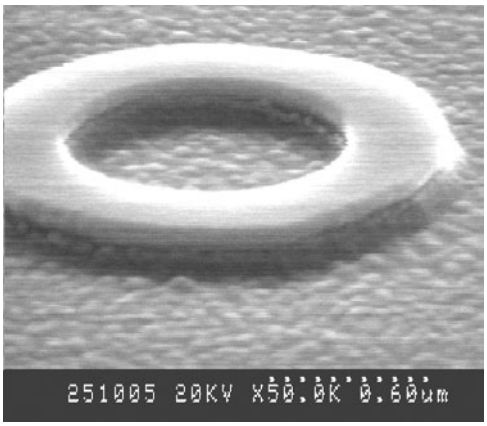

Figure 7. A magnetic ring element after the growth of a Cu/Co/Cu sandwich on top of the prepatterned ring.

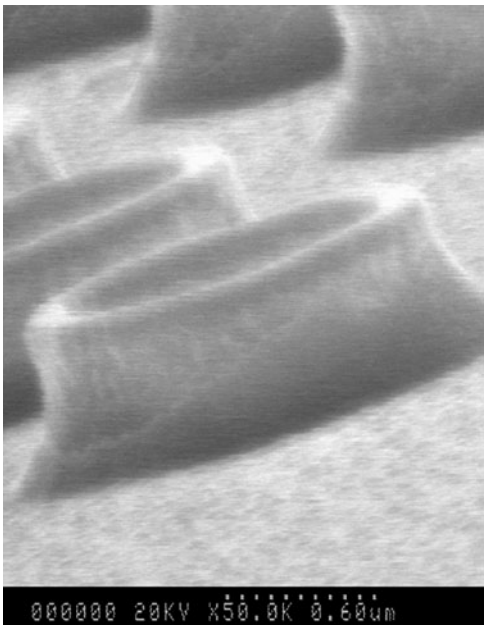

Figure 8. SEM micrograph of rings after deposition. Due to the fast etching of the Si, the ring possesses a significant edge roughness and asymmetry, which influences the magnetic properties of the ring. The flat surface on the top of the rings and the edge of the metallization on the side of the structures indicate that the rings are isolated and well defined.

the side of the structure (figure 8), indicating that the Co on the summit is disconnected from the trenches. Combined scanning transmission electron microscopy (STEM) and electron energy loss spectroscopy (EELS) studies were performed to investigate further the growth and the geometrical definition of the structures. The STEM–EELS measurements were performed with a Vacuum Generators HB501-STEM on a 440 nm diameter and 170 nm high disc, initially milled into a 100 nm slice by focused ion beam (FIB) milling. In figure 9 we show an STEM micrograph of the structure. The use of EELS permits a quantitative determination of the local stoichiometry, as indicated in the figure. This study shows that a special growth mode

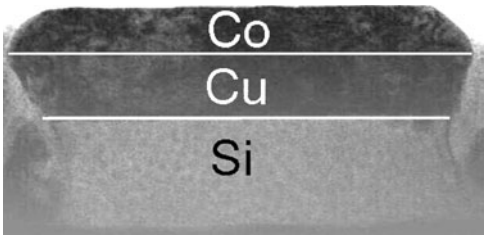

Figure 9. A cross-sectional STEM micrograph after growth on a 440 nm diameter, 170 nm high Si(100) pillar. The chemical identification was obtained using EELS. The light contrast material around the pillar was re-deposited during the ion milling.

of the fcc Cu(100) occurs on the Si(100), which helps to define the structures: the Si pillars are initially undercut and the Cu continues to grow, overhanging in the same direction. When the Co is deposited, the edge profile changes slope, defining a trapezoid-shaped cross-section. The EELS measurements prove quantitatively that no direct exchange between the Co on the summits and in the trenches exists [24]. This means that by using prepatterned substrates, individual free-standing epitaxial rings can be fabricated.

2.2. The lift-off method

With prepatterned substrates, hysteresis loop measurements are difficult as the whole sample is covered with magnetic material and it is not easy to distinguish between magnetic signals from the material on top of the structures and material in the trenches between the structures [3]. A simple fabrication method that overcomes these problems is the lift-off process. Here a patterned polymer resist is coated with a thin magnetic film and is then placed in a solvent to dissolve away the resist, leaving the required patterned magnetic film on the substrate. For this technique to work consistently, the magnetic material on the substrate must be separated from the magnetic material on the resist in order to allow the solvent to reach the resist, and it is important to avoid the deposition of material on the sidewalls, which can remain attached to the substrate after removal of the resist. The deposition of the magnetic film should therefore be normal to the substrate and collimated, and the sidewalls of the polymer resist structures should be vertical or, better still, have an undercut profile. The lift-off process is widely used for producing polycrystalline nanostructures and has been used successfully to produce arrays of magnetic rings [25, 26].

2.2.1. Electron-beam lithography and deposition. A polymethyl methacrylate (PMMA) mask on Si(001) is patterned by electron-beam writing using a LEICA LION LV1 e-beam writer [27]. The machine is run with a low acceleration voltage of 2.5 kV to minimize proximity effects and, with this acceleration voltage, it is possible to pattern a PMMA film with a maximum thickness of 160 nm. The PMMA is developed in MIKB:IPA 1:3 developer. This was followed by the UHV MBE deposition of ferromagnetic materials (Co, NiFe) of varying thicknesses (2–45 nm) and then capped with 2 nm of Au to prevent oxidation. Using resist thicknesses down to 30 nm, we have been able to pattern sub-100 nm rings as seen in figure 10.

2.2.2. Rings with non-magnetic contacts. For the magnetoresistance measurements described in section 5, contacts have to be made to the rings. These rings with contacts were fabricated in a two-step lift-off process. Electron-beam lithography (EBL) using a JEOL 5DIIU nanowriter

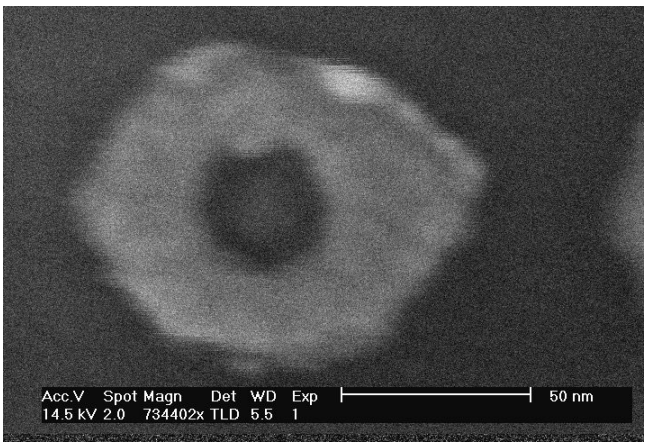

Figure 10. A 10 nm thick NiFe ring with 2 nm Au capping layer. The outer diameter is 90 nm, the inner diameter 50 nm.

was performed at 50 kV accelerating voltage. Firstly, using a 30 pA spot current, rings of 1.5 μm outer diameter and 1.3 μm inner diameter were patterned on a 150 nm thick PMMA resist. In some of the rings, different sized notches were defined in order to leave a small constriction on the ring at the notch positions. This is a very delicate step of the lithographic process because one has to adjust very carefully the local electron-beam dose in order to counter the proximity effects that tend to wash out the notch definition in the resist. The magnetic rings were obtained after deposition and lift-off of permalloy (34 nm) followed by a thin gold capping layer (4 nm). In the second step, contacts were defined again by EBL with a spot current of 1 nA on a 300 nm thick PMMA layer after a very accurate alignment, followed by the lift-off of a Ti(5 nm)/Au(100 nm) bi-layer. The contacts were chosen to be non-magnetic, as otherwise the magnetic states of the ring can be disturbed. A scanning electron microscopy image of such a ring is presented in figure 11. To get a maximum of flexibility for MR measurements, there are six contacts symmetrically distributed around the ring. Each contact is designed so that two wires can be bonded for simultaneous current and voltage measurements allowing for four-probe measurements.

2.3. Nanoimprint

Instead of patterning a resist with electron beams, lift-off structures can also be defined by using nanoimprint to fabricate large arrays of rings. This technique was successfully used by Chen *et al* [28, 29] to fabricate rings from 10 μm diameter down to the submicrometre range. These rings were designed to be not completely round but octagonal to facilitate fabrication and also enable magnetic force microscopy (MFM) imaging of the vortex state [29]. While the resolution and edge definition achieved is not as good as with some of the other techniques described above, nanoimprint nonetheless has the advantage of easy patterning over large areas. An image of an array of rings is shown in figure 12.

3. Morphology and magnetism of thin films

Having discussed the methods used for fabricating our patterned elements, we focus in this section on the common step in all these processes, i.e. the depositions of the metal layers,

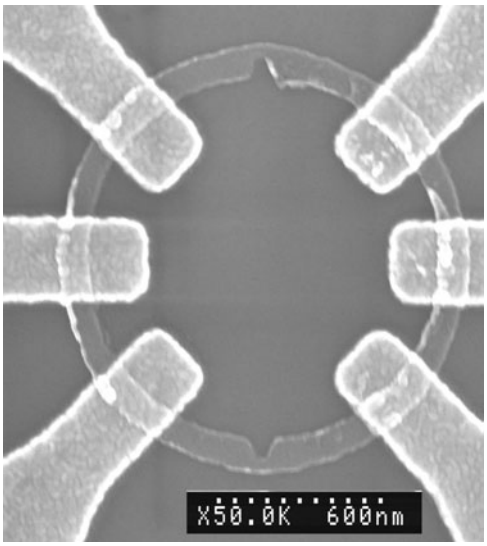

Figure 11. A scanning electron micrograph of a narrow cobalt ring (outer diameter 1.5 μm, inner diameter 1.3 μm). Clearly visible are the six non-magnetic electrical contacts and the two notches.

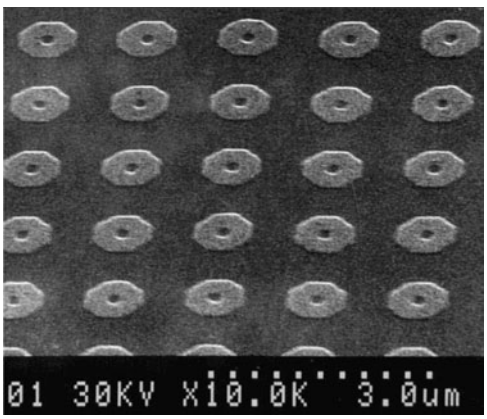

Figure 12. A scanning electron micrograph of an array of rings fabricated using the nanoimprint technique. It can be seen that they have an octagonal rather than a round geometry (by Y Chen, A Lebib, S P Li, M Natali, D Peyrade and E Cambril).

which in our studies are carried out in a UHV MBE system, with a base pressure of the order of 3×10^{-10} mbar. The films deposited onto the substrate can firstly be distinguished in terms of morphology: polycrystalline, if deposited onto an amorphous substrate (e.g., the thermally oxidized Si(001) surface), or epitaxial, if deposited onto a suitably prepared, ordered, surface (such as Cu buffer layers deposited on H-passivated Si(001) substrates, in our studies). This determines to a large extent the magnetocrystalline properties of the resulting structure, namely its macroscopic magnetic anisotropy and the coercivity (i.e., the origin of the pinning sites).

3.1. Polycrystalline films

Polycrystalline films are obtained by deposition of the metal layers onto amorphous substrates, such as the thermally oxidized Si(001) surface. The deposited film consists then of a continuous

agglomerate of small crystallites, whose crystallographic orientation is more or less random along all film directions (otherwise, there will be some degree of texture present). As a consequence, the average magnetocrystalline anisotropy of the film is very small, and the film is magnetically isotropic. In these films, the main sources of pinning sites for domain wall propagation are the grain boundaries of the crystallites, which arise from local variations in strain introduced by the grain boundaries. This usually leads to small coercivities for the continuous films.

3.2. Epitaxial films

Ordered magnetic crystals offer the possibility of studying the effect of the magnetocrystalline anisotropy on the magnetic states of prepatterned small elements. Epitaxial films can be grown by deposition of magnetic materials onto substrates with a small lattice mismatch. This is the case with most 3d transition magnetic metals and the Cu(001) surface. The latter, in turn, can be obtained by depositing a thick Cu layer on H-passivated Si(001) substrates [30–32]. These Cu crystals are not perfect, showing some degree of mosaicity and relatively large roughnesses when compared with suitably prepared Cu(001) single crystals, but they offer many advantages, ranging from ease of preparation to suitability for patterning. The films prepared in this way exhibit the magnetocrystalline anisotropy expected for the single-crystalline bulk materials plus additional anisotropies arising from interface anisotropies, dipolar interactions (shape anisotropy), and strain effects. The overall magnetic anisotropy is the sum total of all these different contributions to the magnetic energy.

3.3. Magnetic properties of Co and NiFe films

In our studies we have considered two different magnetic materials, Co and NiFe (permalloy). The first material allows us to study the effect of the magnetocrystalline anisotropy on the magnetic configurations and reversal processes in small elements, since we can grow either epitaxial or polycrystalline Co. It has also the advantage of having a comparatively large magnetization, increasing the sensitivity of the magnetic measurements. NiFe, on the other hand, has a very small magnetocrystalline anisotropy (the main contribution to the magnetic anisotropy comes from growth-induced effects, and these are of the order of 3×10^4 erg cm^{-3} [33, 34]), providing therefore a very soft magnetic material, often used in practical magnetic devices. It is also one of the materials with the largest anisotropic magnetoresistance (AMR), making it particularly suitable for probing magnetic properties using magnetoresistance (MR). All the NiFe structures fabricated consist of polycrystalline films.

The equilibrium crystal structure of Co at room temperature is the hexagonal close-packed (hcp) structure, and bulk Co has a uniaxial anisotropy with its easy axis along the *c*-direction. However, other metastable crystal configurations can be stabilized by heteroepitaxial growth onto substrates with small lattice mismatches with the phase of interest. One case in point is the fcc phase of Co, which has a lattice constant at room temperature of 3.56 Å (e.g., as extrapolated from the high-temperature lattice constant variation of the equilibrium fcc phase of Co [35]), and which can be stabilized by deposition onto the Cu(001) surface (lattice mismatch of -1.66%). The Co films thus produced are in fact not strictly cubic, but are rather face-centred tetragonal (fct) due to the lattice distortion. This distortion in the lattice structure, due to the biaxial strain exerted by the Cu(001) underlying substrate, has a strong influence on the perpendicular magnetic anisotropy of the Co films (via the magnetoelastic coupling) [36], but less so on the in-plane magnetic anisotropy [37]. As the film thickness

increases, the increase in elastic energy becomes prohibitive, and this energy is balanced by the onset, at a critical thickness, of misfit dislocations (*coherent thickness*, t_c; for Co/Cu(001), $t_c \approx 26$ Å [38, 39]). This introduces local variations in the internal strain in the film, which introduces strong pinning sites for the magnetization (via the magnetoelastic interaction), and is responsible for the relatively large coercivities exhibited by epitaxial magnetic films. As a rule of thumb, we expect the coercive field to decrease with increasing film thickness, since the contribution from this interfacial region is expected to decrease. In single-crystal thin films, the break in symmetry introduces additional anisotropy terms as compared with the bulk case. For materials with cubic crystalline structure, the more general anisotropy expression for thin films includes terms of lower order than cubic; in fact, it is that corresponding to a system with tetragonal symmetry:

$$E_{\text{tetr}} = K_1\alpha_z^2 + K_2^{\perp}\alpha_z^4 + K_2^{\parallel}(\alpha_x^4 + \alpha_y^4) \tag{1}$$

where K_1 corresponds to the out-of-plane anisotropy term (with contributions from shape, magnetoelastic, and surface magnetocrystalline anisotropy), $K_2^{\perp}$ and $K_2^{\parallel}$ to the second-order perpendicular and in-plane anisotropy constants (which are different in the general case), and the α_i are the direction cosines of the magnetization vector. When the magnetization lies in the plane of the film, we may neglect the out-of-plane anisotropy terms, as is the case with thin Co films when the external magnetic field is applied in the plane of the film. The in-plane magnetic anisotropy for Co/Cu(001) has been estimated as $(5\pm1)\times10^5$ erg cm^{-3} [40–42]. Our measured value for a 34 nm thick Cu/Co/Cu/Si(001) film is $(6.5 \pm 1) \times 10^5$ erg cm^{-3} [3, 20], which is comparable to other values reported in the literature and not far from the bulk anisotropy value estimated for fcc Co [43].

Polycrystalline Co films are expected to grow in the hcp phase, but, as mentioned before, due to the random orientation of the crystallites, the magnetic anisotropy averages to zero. The main contribution to the coercivity in these films comes from the grain boundaries between the crystallites, and the average distance between these pinning sites can be identified with the mean crystallite size. It leads to smaller coercive fields than for the fcc epitaxial films.

3.4. Micromagnetic simulations

The magnetization configuration and the switching properties can be simulated using micromagnetic calculations. There are a wide range of programs available using different discretization and solving techniques. In our simulations we solve the micromagnetic equilibrium equation for each applied field on a square mesh with a cell size of 4 nm. A conjugate gradient solver and the OOMMF package [44] were used for the energy minimization and yielded similar results. The necessary material parameters are the saturation magnetization, the exchange constant, and the anisotropy constant. The parameters used for Co are: $K_1 = 6.5 \times 10^5$ erg cm^{-3}, $M_s = 1.424 \times 10^6$ A m^{-1}, $A = 3.3 \times 10^{-11}$ J m^{-1}, and $K_1 = 0$ in the polycrystalline case. For polycrystalline permalloy we used: $M_s = 800 \times 10^3$ A m^{-1} and $A = 1.3 \times 10^{-11}$ J m^{-1}.

4. Magnetic states

One of the main areas of interest in small magnetic structures arises from the influence of the shape of the element on the magnetic states and the switching behaviour. So the first step when investigating a new geometry is to consider what stable magnetic states are permitted by that geometry. In the case of the ring shape, the magnetization will predominantly follow the circumference to minimize the stray field, leading in the simplest situation to a complete

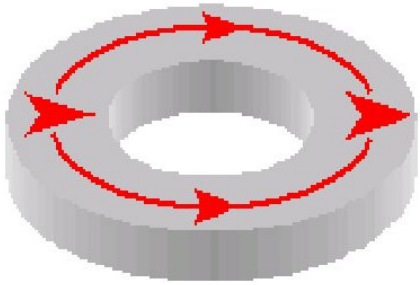

Figure 13. A schematic representation of the onion state. The magnetization has opposite senses of circulation in the two halves of the ring and two head-to-head domain walls are formed.

flux-closure vortex state (with clockwise or anticlockwise circulation of the magnetization). In contrast to the disc geometry where the vortex state is unfavourable in small elements due to the high exchange energy of the vortex core, in rings the vortex core is removed giving a very stable vortex state (figure 1). At saturation, the rings are forced into a single-domain state, and as the field is reduced the magnetization follows the circumference of the ring and forms the so-called 'onion' state (figure 13)—so called as it resembles an onion sliced from top to bottom—which is characterized by two head-to-head domain walls [3]. To theoretically predict which states are stable, we have to consider the energy contributions from the exchange, anisotropy, and stray (demagnetizing) fields [45]. Local minima in the total energy correspond to accessible stable (or metastable) states of the system.

Qualitatively, the stray field energy term always favours a vortex state with a closed flux, while the exchange interaction favours a single-domain state. As the stray field energy is dependent on the square of the thickness, while the exchange energy increases linearly with the thickness, one would expect for thick films the vortex state and for thin films the onion state to be favourable. If there is a sufficiently large uniaxial anisotropy present, again the onion state is favoured [45]. A cubic anisotropy will change the magnetic states as well, as discussed in detail below (section 4.1).

Different techniques have been used to image the magnetization configurations. The stray field has been measured using scanning Hall probe microscopy [46] and different groups have used magnetic force microscopy (MFM) [29, 47, 48]. We chose photoemission electron microscopy (PEEM) and scanning electron microscopy with polarization analysis (SEMPA), which are non-intrusive techniques, in contrast to imaging techniques such as MFM (as shown in the imaging of octagonal structures, MFM can influence and even switch the magnetic configurations [29]). Furthermore, unlike MFM, the non-intrusive techniques used here allow us to even image magnetic states with no stray field such as the vortex state.

PEEM was carried out at the synchrotron ELETTRA in Trieste [49]. In x-ray magnetic circular dichroism photoemission electron microscopy (XMCDPEEM) the yield of secondary electrons created by excitation with circularly polarized light depends on the dot product $\vec{P} \cdot \vec{M}$ of the polarization $\vec{P}$ and the magnetization direction $\vec{M}$. The secondary electrons are used for imaging by a spectroscopic photoemission and low-energy electron microscope (SPELEEM) and the yield difference is visible as magnetic contrast in the images [49]. To achieve a higher resolution than that possible with MFM or PEEM, SEMPA was performed at the National Institute of Standards and Technology (NIST) [50]. The sample is introduced into a UHV chamber and the sample capping layers are sputtered off. A high-energy electron beam is focused onto the sample surface and the intensity and spin polarization of the emitted secondary electrons are measured, enabling simultaneous imaging of the topography and magnetization.

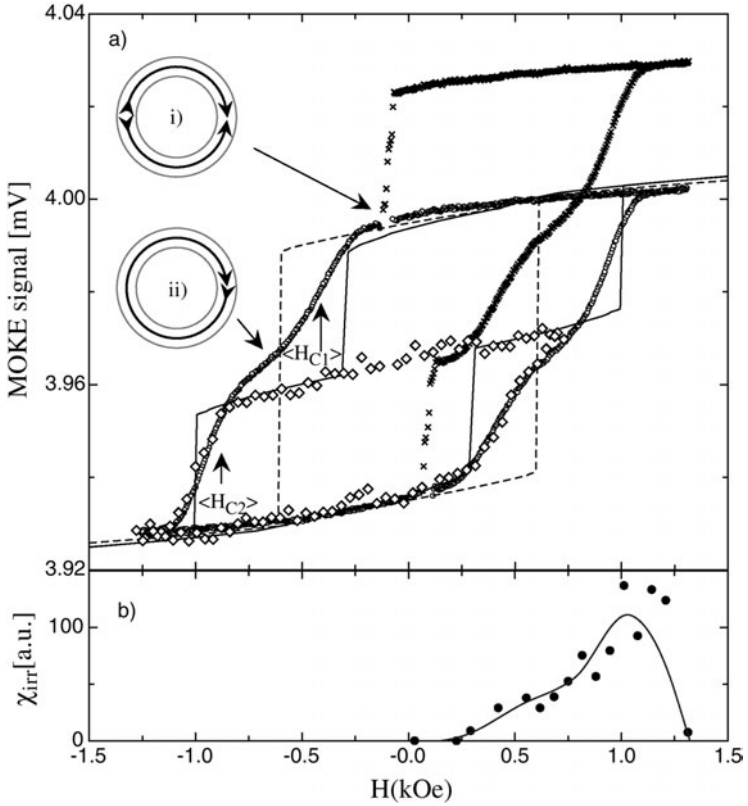

Figure 14. (a) Hysteresis loops of $d_{\rm int}/d_{\rm ext} = 1.3\ \mu$m/1.6 μm epitaxial fcc Co ring magnets. The open circle curve is the corrected loop for the rings obtained from the measured MOKE data (crosses). The dashed and solid lines represent the simulations of a symmetric ring and an asymmetric ring, respectively. The cartoons are schematic diagrams of (i) the onion state and (ii) the vortex state, which occur as indicated by the arrows. The diamonds represent an asymmetric minor loop achieved from saturation in negative fields. (b) The measured irreversible susceptibility: for each minor loop obtained at a given maximum field $H_{\rm max}$, the irreversible change in the magnetization $\Delta M_{\rm irr}$ was determined. The quantity $\mathrm{d}\,\Delta M_{\rm irr}/\mathrm{d}H_{\rm max}$ provides an estimate of the irreversible susceptibility $\chi_{\rm irr}$. The continuous line is a guide to the eye.

Both orthogonal magnetization components within the plane of the sample are measured, so the magnitude and direction of the in-plane magnetization are completely determined. The probing depth of the secondary electrons is limited to approximately 1 nm, making this technique as a sensitive surface magnetometer. The results can then be compared with micromagnetic simulations.

4.1. Observation of magnetic states in rings

In figure 14 we show magneto-optical Kerr effect (MOKE) measurements performed on an array of rings with $d_{\rm int}/d_{\rm ext} = 1.3\ \mu$m/1.6 μm (34 nm thick, epitaxial fcc Co). The crosses correspond to the as-measured loop, which includes the contribution from the trenches (with the low switching field). When this contribution is removed, we obtain the magnetic signal from the rings only (circles). Two transitions are observed, one from a high-magnetic-moment state obtained after relaxing the field from saturation to the low-magnetic-moment state and

then to the reverse high-magnetic-moment state. Minor loops starting from saturation in one direction were performed to investigate the nature of the two transitions and to estimate the irreversible susceptibility. The diamonds in figure 14 represent a minor loop where the maximum positive applied field was intermediate between the two transition fields (H_{C1}, H_{C2}). We note that the change of the magnetization is very small away from the transition and that the remanence is zero. The reverse transition occurs at an applied field corresponding precisely to $-H_{C2}$. This shows that transition 1 is a switch from the first high-moment stable state into a second low-moment stable state. The second state has zero remanent magnetization, and subsequently switches back to the first state independently of the applied field direction. From this we conclude that this second state must correspond to the vortex state. Further, minor loops for smaller maximum positive applied fields than that used in obtaining the minor loop in figure 14(a) show the same transitions. Therefore, all irreversible processes in the vicinity of H_{C1} correspond to direct transitions into the vortex state without stable intermediate states. The measured irreversible susceptibility is shown in figure 14(b) and is seen to be zero before the first transition. Hence, the first state is reached reversibly from saturation. This implies that as the field is decreased the flux must be closed on each half of the ring defining the onion state with two opposing head-to-head walls, as schematically represented in the figure.

In figure 15(a) we present a hysteresis loop of an array of polycrystalline rings (outer diameter $d_{\text{ext}} = 1200$ nm, inner diameter $d_{\text{int}} = 900$ nm, and thickness $t = 15$ nm; polycrystalline Co). They show essentially the same behaviour as the epitaxial rings in figure 14, though the switching field distribution is reduced as compared to the epitaxial and single-crystalline rings. To obtain direct evidence of the actual magnetization configurations (onion state, vortex state) we directly image these rings using PEEM. We make use of the fact that we measure an array of rings with a switching field distribution. So we can switch some of the rings into the onion state while some will remain in the vortex state by following the field path indicated by the red arrows in the hysteresis loop in figure 15(a), where the field is relaxed to zero from the value corresponding to the middle of the switching field distribution of the vortex-to-onion transition [3]. A low-resolution PEEM image of four rings (outer diameter $d_{\text{ext}} = 1100$ nm, inner diameter $d_{\text{int}} = 850$ nm, and thickness $t = 15$ nm; polycrystalline Co) at remanence is shown in figure 15(b). As expected, some rings are still in the vortex state (two rings have an anticlockwise and one ring has a clockwise circulation direction) while one ring has already switched into the onion state. While it is easy to confirm the vortex and onion states with PEEM, the maximum resolution achieved (30 nm) is not sufficient to resolve the details of the exact magnetization configuration such as the structure of the head-to-head domain walls in the onion state. Since micromagnetic simulations predict different types of head-to-head domain wall [51] and since the type of domain wall is important in particular for the switching behaviour [52] and for the nucleation-free onion-to-vortex transition [3], we have chosen to carry out more detailed high-resolution imaging using SEMPA. For epitaxial samples with a cubic anisotropy, micromagnetic simulations predict that, in addition to the head-to-head domain walls that are also present in the onion state of polycrystalline rings, epitaxial samples should show additional domain features in the magnetization configuration. Furthermore, epitaxial samples of different geometries also allow the study of the interplay between the magnetocrystalline anisotropy and the local shape anisotropy due to the dipolar interactions. A SEMPA image for a wide epitaxial ring ($d_{\text{ext}} = 1600$ nm, $d_{\text{int}} = 900$ nm, $t = 34$ nm; fcc Co) is shown in figure 16(a). In this wide ring the head-to-head wall is a vortex wall, since this minimizes the stray field at little cost from the exchange energy term as theoretically predicted [51]. The micromagnetic simulation in figure 16(b) shows remarkable agreement, although the exact position of the head-to-head domain wall in the experiment is

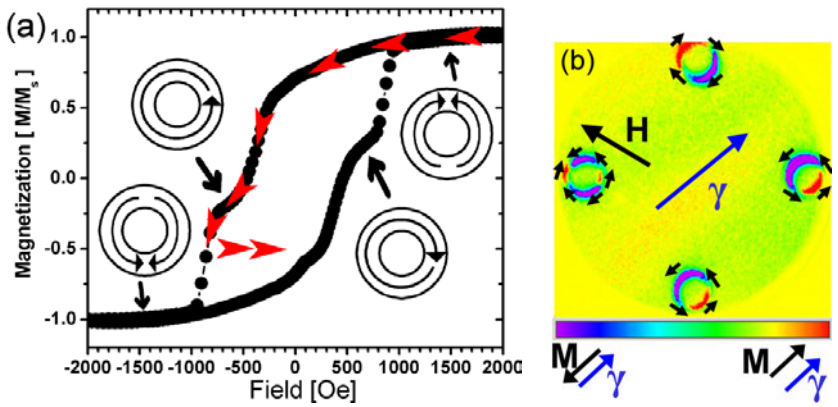

Figure 15. (a) The hysteresis loop measured on an array of rings (outer diameter $d_{\text{ext}} = 1200$ nm, inner diameter $d_{\text{int}} = 900$ nm, and thickness $t = 15$ nm; polycrystalline Co). The magnetization configurations of the onion and the vortex states are shown schematically. Red arrows indicate the field path used to obtain the rings in the states imaged with PEEM in (b). (b) A PEEM image of four polycrystalline Co rings. The top ring attains the clockwise vortex state, the bottom and right rings attain the anticlockwise vortex state, and the left ring is in the onion state pointing along the direction of the applied field H. The field of view is ≈ 10 μm across and the blue arrow points in the direction of the photon beam. The colour scale indicates the direction of the magnetization with reference to the direction of the incoming photon beam (magnetization parallel to the incoming photon beam (red) to antiparallel (purple)).

determined by local defects (the highly energetic vortex core is pinned at non-magnetic defects). In addition to the head-to-head walls, a domain structure is visible in both the SEMPA image and the simulation, demonstrating the influence of the magnetocrystalline anisotropy for this wide-ring geometry.

In narrow rings any deviation of the magnetization direction from parallel to the ring edge will create dipole stray fields. Therefore the magnetization closely follows the shape (local shape anisotropy) and aligns with the circumference. This means that no domain features are expected as the strong local shape anisotropy overcomes the magnetocrystalline anisotropy. This can be seen in the SEMPA image in figure 16(c) and in the micromagnetic simulation in figure 16(d) of a narrow ring ($d_{\text{ext}} = 1600$ nm, $d_{\text{int}} = 1200$ nm, $t = 34$ nm; fcc Co). Furthermore, in this narrow ring, as expected from energy considerations, a transverse head-to-head domain wall is present since a vortex wall would have to be compressed into the narrow ring resulting in a prohibitively high exchange energy. Our results are in good agreement with the wall types predicted in [51] from micromagnetic simulations. The energetics of the different domain wall types are analysed further in [51] as well. In addition to the vortex and onion states, that are found at remanence, very wide rings in an applied field also exhibit an additional 'vortexcore' state, where a complete vortex core is present in the ring as seen in the micromagnetic simulation in figure 17 and explained in detail in [24].

4.2. Remanent magnetic states in epitaxial Co nanoscale discs

Discs can be seen as the limit of very wide rings. The general magnetic properties of the disc geometry have been widely investigated (e.g. in [5]), so we will focus here on special aspects such as the domain walls that are found in epitaxial discs with a cubic anisotropy. Using SEMPA we investigate the magnetic nanostructure of epitaxial fcc Co/Cu(001) circular elements [53]. From a fundamental point of view, the study of epitaxial magnetic mesoscopic systems allows

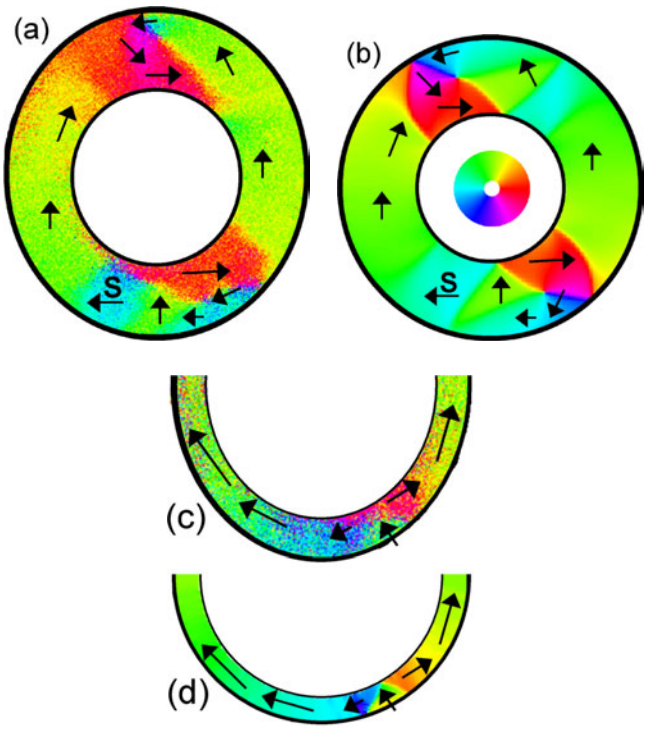

Figure 16. Micromagnetic calculations and SEMPA images of the onion state in a wide ($d_{ext} = 1700$ nm, $d_{int} = 900$ nm) and a narrow ($d_{ext} = 1700$ nm, $d_{int} = 1200$ nm) epitaxial 34 nm thick fcc Co ring. (a) SEMPA image of the wide ring. The vortex walls and the magnetocrystalline anisotropy-induced domain structure (marked with S) are visible. (b) A micromagnetic simulation of the wide ring. In addition to the vortex head-to-head domain wall, the domain structure is visible (marked with S). The position of the vortex core is slightly different from that in the SEMPA graph, as in the experiment the position is determined by non-magnetic defects that pin the vortex core, which are absent in the simulation. The colour code indicating the direction of the magnetization is shown. (c) SEMPA image of the narrow ring (only half the ring is shown). No domain structure is seen as the local shape anisotropy dominates over the magnetocrystalline anisotropy. A transverse head-to-head domain wall is present. (d) A micromagnetic simulation of the narrow ring exhibiting the transverse domain wall.

the study of the role of anisotropies in the equilibrium magnetic configuration. Also, the stable magnetic configuration is strongly dependent on the geometry of the element [1, 3–7] and on the strength and orientation of the magnetocrystalline anisotropy, which in turn determine the reversal mechanism of the magnetization.

The 34 nm thick fcc Co discs were fabricated as described in section 2.1. The outer diameter was fixed at $\sim$1.7 μm and the separation between the elements was set to 6 μm. MOKE magnetometry measurements were performed on similar samples [3]. The magnetic domain structure of the elements was imaged at remanence with SEMPA, and images for two of the array of discs are shown in figure 18. The bottom disc presents a closed flux configuration typical of a system with cubic anisotropy, with the magnetization inside each domain oriented along the $\langle 110 \rangle$ direction, which corresponds to the easy magnetization axis of fcc Co. This is the prevalent state observed for the discs. The domain configuration shown in the top disc of figure 18 is more complex, although still resembling a closed flux configuration. The disc has a net magnetic moment since one of the domains is larger than the others, corresponding

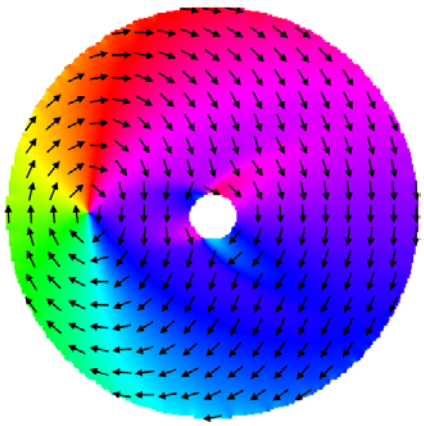

Figure 17. Micromagnetic simulation of the 'vortexcore state' where a complete vortex core is present in the ring. This state only exists in very wide and thick rings in an applied field.

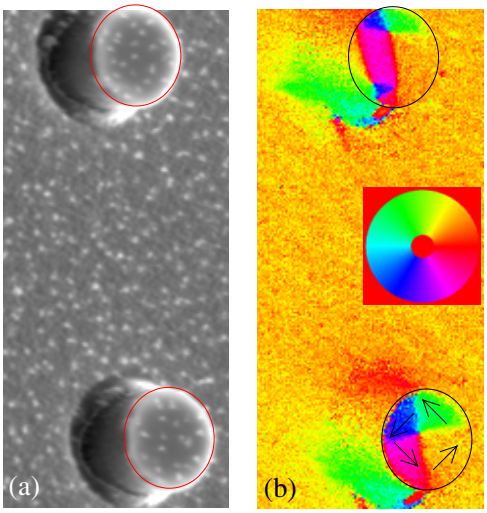

Figure 18. SEMPA images of two discs. (a) The topography of the discs (SEM) showing the nanopillars rising well above the background and where the clear physical separation between the magnetic material deposited in the trenches and the mesas can be appreciated. (b) Magnetic contrast. Because of the geometry of the measurement, the magnetization data just to the left of the disc are in the shadow of the detector and should be ignored. The inset shows the key to the orientation of the magnetization (pointing outwards).

to the direction along which the field was applied. Micromagnetic simulations were carried out for comparison, with the discs being saturated along one magnetic easy axis and allowed to relax under no applied field.

4.3. Geometrically constrained domain walls

Of particular interest is the study of the equilibrium magnetic states and magnetization reversal mechanisms in small elements, which are strongly determined by the interplay of the different anisotropy terms with the physical shape of the element. The magnetic anisotropy is expected

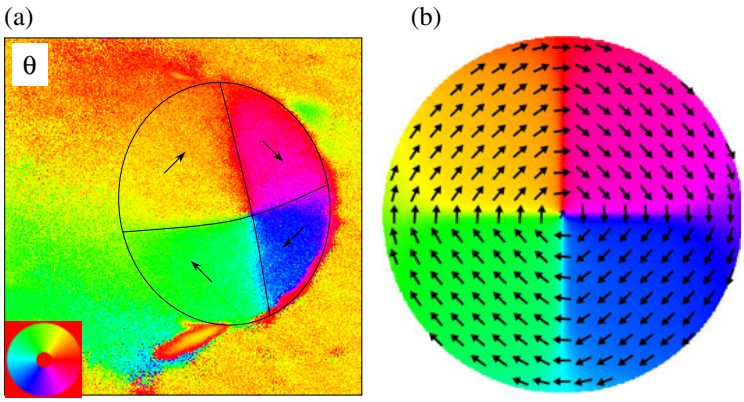

Figure 19. (a) SEMPA image of a disc with a quadrant state for higher-magnification SEMPA. (b) The equilibrium state obtained from a micromagnetic simulation. The magnetization direction is given by the colour, keyed to the inset colour wheel.

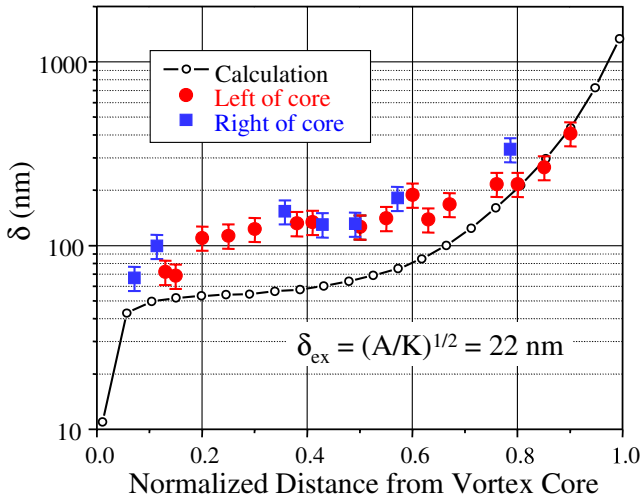

Figure 20. Variation of the domain wall width as a function of the normalized distance from the vortex core.

to play an important role in determining the equilibrium magnetic states and ultimately the reversal of the magnetization process. In general, the effect of the magnetic anisotropy is to restrict the states with flux closure to those compatible with local domains pointing along the easy direction axis. Less clear, however, is how the magnetocrystalline anisotropy and the dipolar interactions (i.e., shape of the element) together determine the form and extent of the effective transition at a magnetic domain boundary in small elements. More generally, there is strong current interest in the concept of a geometrically constrained domain wall [54].

A higher-magnification image of one of the discs, shown in figure 19, allows a closer look into the details of the four-quadrant domain structure. Simulations show that, after saturation in an in-plane magnetic field, the dominant remanent equilibrium state is the quadrant state, as observed experimentally. The domain formation occurs by nucleation of two vortex cores on two opposite edges of the disc where the magnetostatic energy is maximum (i.e., at the ends

of the dipole defined by the saturated state). The vortices need not occur simultaneously, and one may have a smaller nucleation energy and propagate throughout the disc, thus creating the quadrant state. When two vortices are created (as observed in our simulations), one of the vortices moves to the centre of the disc and pushes the other outwards until it vanishes. In some few instances, it may happen that these vortices are pinned by defects, and are still present in the remanent state as observed in some of the discs (top right disc of figure 18). The width of the domain wall is the result of the energetic compromise between the exchange, anisotropy, and dipolar interaction terms: while close to the perimeter of the disc the magnetization minimizes the free magnetic poles by remaining parallel to the perimeter, in the centre of the disc the spins try to orient along the magnetocrystalline easy axes. This results in a rather wide, geometrically constrained domain wall, whose width decreases from the outside towards the centre of the disc; see figure 20. (The experimental data suggest that the variation of the domain wall width scales with the distance between the vortex core and the disc radius.) For small distances from the centre the DW width assumes a value close to $\frac{\pi}{2}(A/K)^{1/2}$ while at the periphery of the disc it assumes a value close to the geometrical parameter $r_0\pi/2$ corresponding to a circular magnetization configuration (where r_0 is the disc radius). The situation in this case is analogous to the case of edge curling walls in patterned elements [55–57] and resembles also the equivalent in thick films of domain walls in closure domains [58], where minimization of the magnetic energy is achieved by extended domain walls that may reach the periphery of the element or the surface of the film, respectively. The experimental values show the same trend as the calculations, a plateau followed by an upturn in the domain width with increasing distance from the vortex core, although the value of the domain wall at the plateau is a factor of two larger than that predicted by the simulations. This discrepancy may be due either to a smaller magnetocrystalline anisotropy constant than that measured in continuous films or to a larger exchange constant than that assumed in the calculations (or a combination of these two factors).

5. Switching

So far we have completed the first step in the investigation of the magnetic properties by finding out which equilibrium states exist, and using MOKE measurements [3] we have examined which transitions occur in rings with different geometrical parameters. The next step, namely obtaining the details of the actual switching processes, has to be primarily theoretical, since nanometre and picosecond scale space- and time-resolved measurements are very difficult. Micromagnetic simulations can give a good indication of the dynamics of the reversal process, in particular when the original and final magnetic states as well as the switching fields agree with the experimental results. Recent temperature-dependent measurements [59] have shown that at low temperatures pinning becomes more important and switching fields are larger than the values predicted by micromagnetic simulations. This is due to the fact that simulations do not include any defects apart from the natural edge roughness due to the cell discretization. Here we explain in detail the physical processes happening during the reversal. Systematic studies of the switching fields as functions of the geometrical parameters can be found in [60, 61]. There it is shown in detail that the onion-to-vortex transition in very wide and thick micron-sized rings (700 nm wide, 34 nm thick Co) can occur before reaching zero when reducing the field, while in the narrowest and thickest ($<$100 nm wide, 40 nm thick Co) rings, opposite fields of up to 500 Oe have to be applied before the transition occurs. For the vortex-to-onion transition, wide and thin rings ($\approx$10 nm Co) can switch at less than 300 Oe, whereas thick and narrow rings exhibit switching fields of more than 2000 Oe.

5.1. Onion-to-vortex transition

5.1.1. Onion-to-vortex switching process. We consider first the onion-to-vortex transition. In order to study the effect of shape fluctuations on the switching process, we have performed micromagnetic simulations of both a perfectly symmetric ring and also an asymmetric ring where the width of the ring changes slightly from one side to the other. Hysteresis loops were computed by solving the micromagnetic equilibrium equation for each applied field as described before [11]. The hysteresis curves obtained from the simulations are compared to the experimental results in figure 14. For the symmetric ring we only observe one transition: the ring switches directly from one onion to the reverse onion state without going into the vortex state. The switching mechanism in this case is surprisingly simple and close to domain wall motion. The two walls start to move simultaneously in the same rotational direction, so they chase each other around the perimeter of the ring. The onion state is completely switched when the walls have reached the opposite side. However, if asymmetries are present in the ring, as in our experiments, the simulations show that the walls will not start to move simultaneously. One wall will be more strongly pinned than the other, and a transition into a vortex state will take place when the other wall has depinned and moved toward the pinned wall, resulting in the annihilation of both walls. This is illustrated in figure 14, where two transitions are observed for the asymmetric ring. Figure 21 shows snapshots of the first transition in figure 14. The simulated switching field for the onion-to-vortex transition, $H_{C1} = 350$ Oe, falls well within the distribution of the experimental values.

In our simulations we assumed a smooth, gradual variation of the ring width, which acts as a smooth potential for the wall with an energy minimum at the narrow end, as illustrated in figure 21. This model leads to nucleation-free switching as discussed above. To test this model further, we have performed simulations for rings with one small notch, representing the asymmetry which traps one of the walls, showing that in this case also, a nucleation-free onion-to-vortex transition, identical to that obtained for the smooth asymmetric ring, occurs. We infer that the exact nature of the asymmetry does not influence the switching mechanism for the onion-to-vortex transition in these narrow rings, although the specific switching field is affected. Finally, we note the quantitative agreement between the values of the observed and the simulated switching fields and that the onion-to-vortex transition is observed to occur without forming any other intermediate stable state (though this might not be true for all ring geometries [47]).

5.1.2. Influence of magnetocrystalline anisotropy. An additional question is that of how the onion-to-vortex transition is affected by the presence of a magnetocrystalline cubic anisotropy [62]. Quasi-static hysteresis loops along the magnetocrystalline easy and hard axes have been computed for asymmetric rings with external and internal diameter $d_{\text{ext}} = 1.6\ \mu$m, $d_{\text{int}} = 1.3\ \mu$m, respectively, and thickness $t = 34$ nm of fcc Co. Figure 22 shows the first jump (onion-to-vortex transition) in the hysteresis loop along the magnetocrystalline hard (solid line) and easy (dashed line) axes. We see that the switching field is significantly higher along the hard axis. This is a consequence of the interaction between magnetocrystalline anisotropy and demagnetizing fields in the particular geometry of the rings and can be understood as follows. The onion state is more stable when the field is aligned along the magnetocrystalline hard axis, as schematically represented by the arrows in diagram (a) of figure 22. In contrast, when the field is applied along the magnetocrystalline easy axis, the onion state is less stable (in this case the arrows would be oriented along hard directions) and a smaller field is required to depin the walls. Furthermore, the intermediate state observed in the easy axis loop in figure 22 corresponds to the state in which the wall that depins first (the one on the right) has moved from

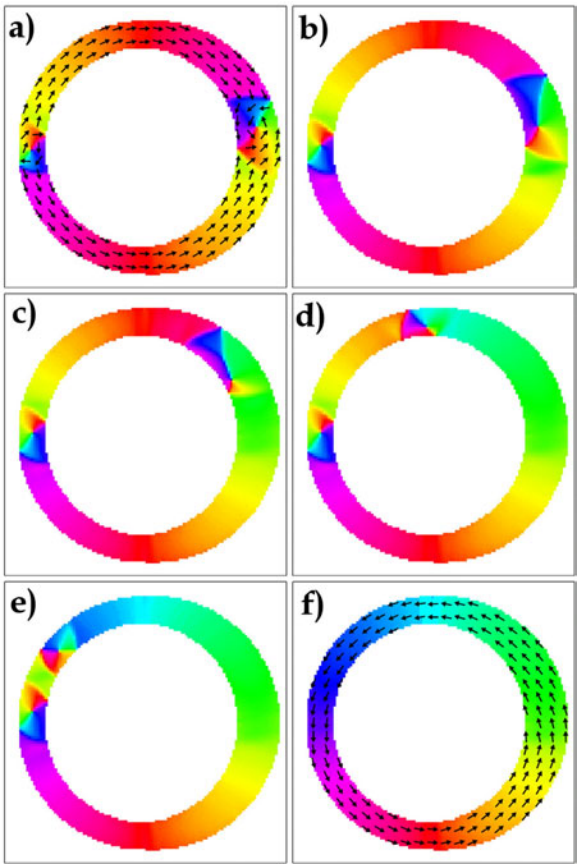

Figure 21. Illustration of the onion-to-vortex switching in an asymmetric ring. The snapshots (a) and (f) are of equilibrium states before and after the switching and snapshots (b) to (e) are of intermediate states during the switching. The colour scale indicates the horizontal component of the magnetization in the plane, as illustrated by the arrows in (a) and (f).

its original position and is now pinned at 45° from the applied field direction (horizontal), which allows the orientation of the spins along easy axes, as represented in diagram (b). Therefore, it is found that in magnetic rings the magnetocrystalline hard axis becomes the global easy axis and vice versa. This effect is usually washed out in experiments due to edge imperfections and film roughness.

5.2. Vortex-to-onion transition

5.2.1. Vortex-to-onion switching process. In this section we investigate the vortex-to-onion transition from micromagnetic calculations of first-magnetization curves [11]. Since at remanence the lowest energy state in these rings is the vortex state, first-magnetization curves start with the ring in the vortex state and then the magnetic configuration, with increasing field, is computed. Of particular interest here is the critical field where the switching occurs and the vortex state is destroyed. Calculations of complete hysteresis loops give exactly the same switching fields for the vortex-to-onion transition as the first-magnetization curves, so either can be used to investigate the switching fields. We chose to use first-magnetization

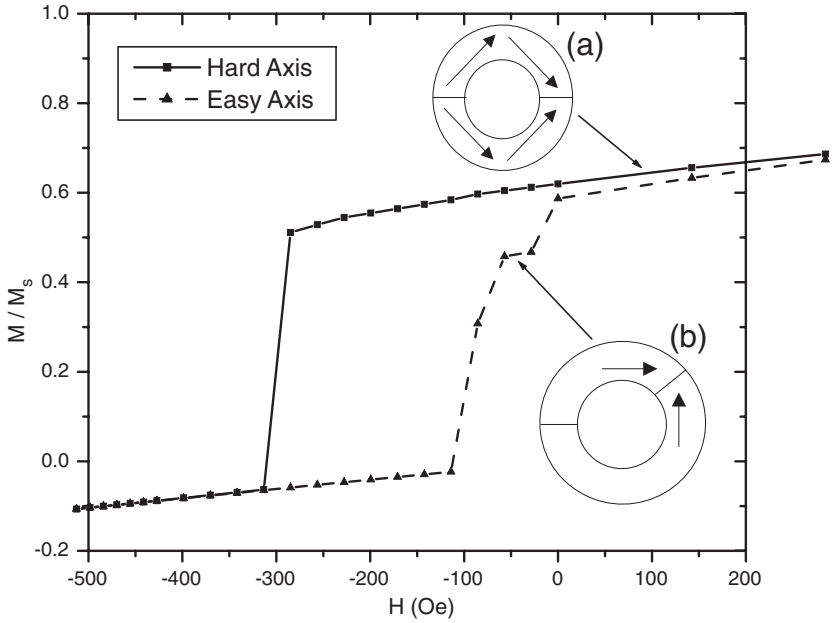

Figure 22. The first jump in the hysteresis loop, corresponding to the transition from onion to vortex, along the easy (dashed line) and hard (solid line) axes. The magnetization configuration in the onion (a) and the intermediate state along the easy axis (b) are shown schematically. The field is applied along the horizontal direction in both cases.

curves instead of complete hysteresis loops as this connects with our previous work [11] and it also reduces computation time. The first-magnetization M–H loops were computed by solving the micromagnetic equilibrium equation for each applied field on a square mesh as explained before. A simulated first-magnetization M–H loop is presented in figure 23 and the corresponding magnetization configurations are shown in figure 24(a), which shows the ring in the vortex state at zero field. As the applied field is increased, the spins rotate slightly but the rings remain in the vortex state as seen in figure 24(b). At the critical field a reverse domain is nucleated at the edge of the ring (seen in blue in figure 24(c)). This domain then grows in size and gradually propagates along the perimeter of the ring and outwards (figures 24(d), (e)) until the ring attains the onion state (figure 24(f)). As the applied field is further increased, the onion state reversibly approaches saturation. Although the propagation process involves non-uniform states for which the details of the predicted domain structure can depend on such parameters as the cell size, it is found that the key property, namely the critical field where the first nucleation of a reverse domain occurs, is relatively insensitive to the cell size [11]. Our simulations suggest that the vortex-to-onion transition is not significantly affected by magnetocrystalline anisotropy. This suggests that the nucleation field is primarily shape dependent.

5.2.2. Vortex circulation direction. Here we focus on the influence of the switching mechanism on the circulation of the vortex state. After reducing the field from saturation, the rings attain the onion state at remanence. In the simulation we introduced a notch to pin one of the walls more strongly than the other (to simulate the real case, such as the rings discussed in this section, where asymmetric pinning is observed even without artificially introduced asymmetries, due to the fact that the rings are never absolutely symmetrical [3]). In addition,

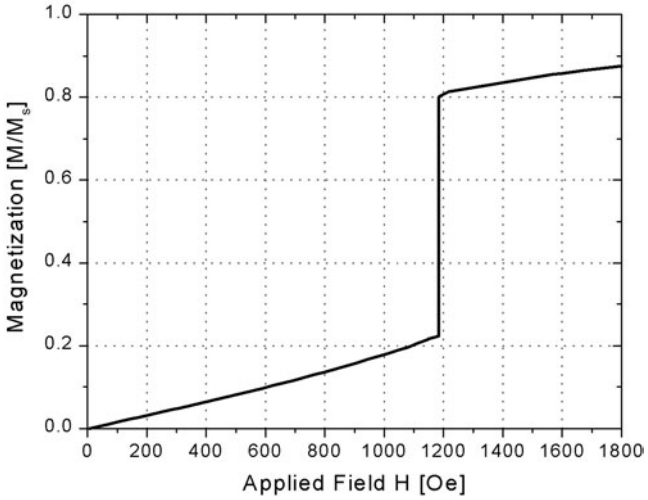

Figure 23. The first-magnetization curve for a cobalt ring with outer diameter 1870 nm, ring width 195 nm, and a film thickness of $t = 34$ nm showing a critical field of $H_c = 1180$ Oe.

the exact positions of the two domain walls are determined both by the magnetocrystalline anisotropy and by pinning due to geometrical features and will, in an experiment, always be misaligned with respect to the applied field. Therefore, in the simulation we misaligned the field with respect to the equilibrium position of the domain walls, defined by the anisotropy and the position of the notch, as shown in figures 25(a) and (c). Due to this misalignment the applied field will exert a force on the walls. As the wall without the notch is pinned less strongly, it will depin at a lower field than the other, and it will start to move in the direction indicated by the arrow. When it arrives at the notch it will annihilate with the pinned wall. This nucleation-free switching process yields the vortex states shown (one is clockwise; the other one is anticlockwise). Hence, these simulations show that a particular vortex state can be prepared using a uniform field to switch the rings from the appropriate onion state into the desired vortex state.

A direct experimental confirmation of the vortex circulation control is difficult, as the two vortex states cannot be distinguished using measurements of the total magnetization of a complete ring. However, when looking with a Kerr microscope at the magnetization of approximately half of a ring, as shown in figure 26(a), the longitudinal hysteresis loops show a clear difference. In figure 26(b) the black hysteresis loop shows a simulation for the magnetization of the right half of a ring that reverses by falling into different vortex states in each branch of the loop ($A \xrightarrow{1} B \xrightarrow{2} C \xrightarrow{3} D \xrightarrow{4} A$). Jump 1 from the onion state A to the clockwise vortex state B and jump 3 from the reverse onion state C to the anticlockwise vortex state D correspond to large jumps in the magnetization, as the magnetization in the right half of the ring reverses completely. Jumps 2 and 4 are small jumps, as the magnetization of the right half of the ring hardly changes. The difference in height between the jumps 1 and 2 (or 3 and 4, respectively) depends on which part of the ring is illuminated (in our case just over half of the ring) with respect to the direction of the applied magnetic field. However, it is important to note that the loop is always symmetric.

Using the heights of the jumps from the black loop one can construct a hypothetical loop (shown in grey in figure 26(b)) for a ring that reverses by falling always into the same vortex state ($A \xrightarrow{1} B \xrightarrow{2} C \xrightarrow{5} B \xrightarrow{6} A$). This loop shows instead of the large jump 3 the small

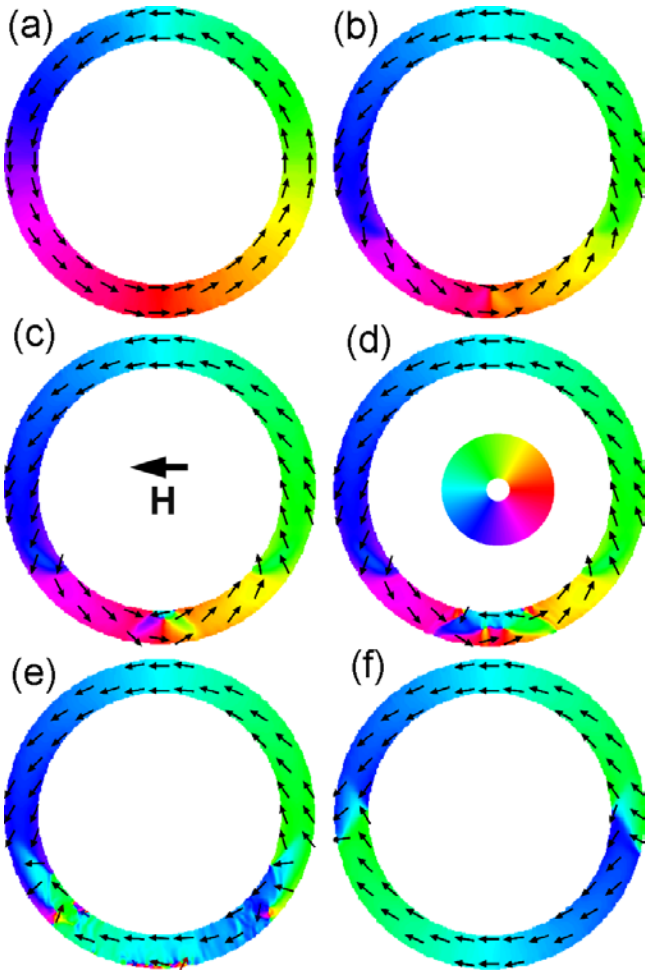

Figure 24. Magnetization configurations of the ring used for figure 23 at different applied fields. (a) 0 Oe (vortex state); (b) 1170 Oe (just before switching); (c), (d), (e) 1180 Oe (during the switching); (f) 1200 Oe (onion state). Parts (a), (b) and (f) show equilibrium states whereas (c), (d), (e) are snapshots of the dynamics of the reversal. The direction of the applied field is indicated and the colour code for the magnetization directions is presented.

jump 5 when the loop goes from the reverse onion state C back to the clockwise vortex state B. Then jumping back to the onion state A yields a large jump 6. The asymmetry of the grey loop is striking, as there is a large difference in heights between jumps 1 and 5 (or 2 and 6, respectively). From the asymmetry in the hysteresis loop it is possible to identify rings that reverse by switching into the same vortex.

We investigated an array of prepatterned epitaxial fcc Co(001) rings, having an outer diameter $d_{\text{ext}} = 1.8\,\mu$m, an inner diameter $d_{\text{int}} = 1\,\mu$m, and a thickness of 34 nm. The magnetic measurements were performed using scanning Kerr microscopy [63] with a resolution smaller than 4 μm and a scanning step size of 0.1 μm. Details of the measurements are presented in [19]. All the observed loops are symmetric, thus proving that the rings indeed fall into a different vortex state depending on the onion state that the transition starts from. So, most importantly, we have shown that the sign of the onion state uniquely determines the vortex

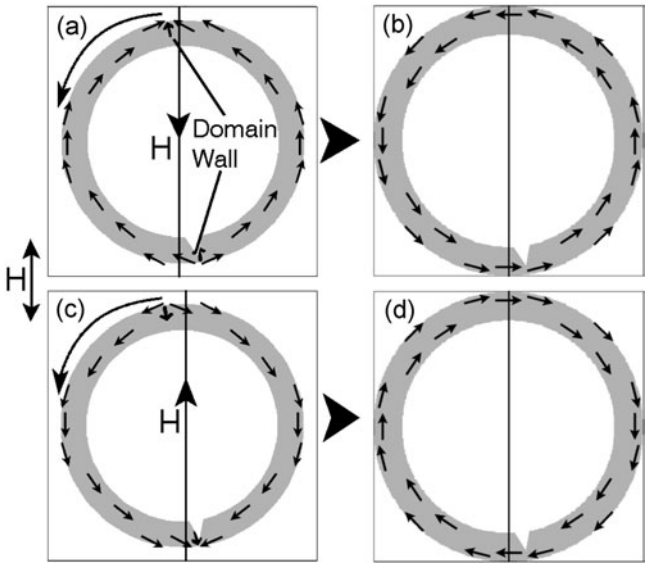

Figure 25. Rings in the two onion states (left) and after switching to the resulting vortex states (right). The lower domain wall in the onion state is the more strongly pinned wall due to the notch. The curved arrow indicates the direction of the domain wall motion.

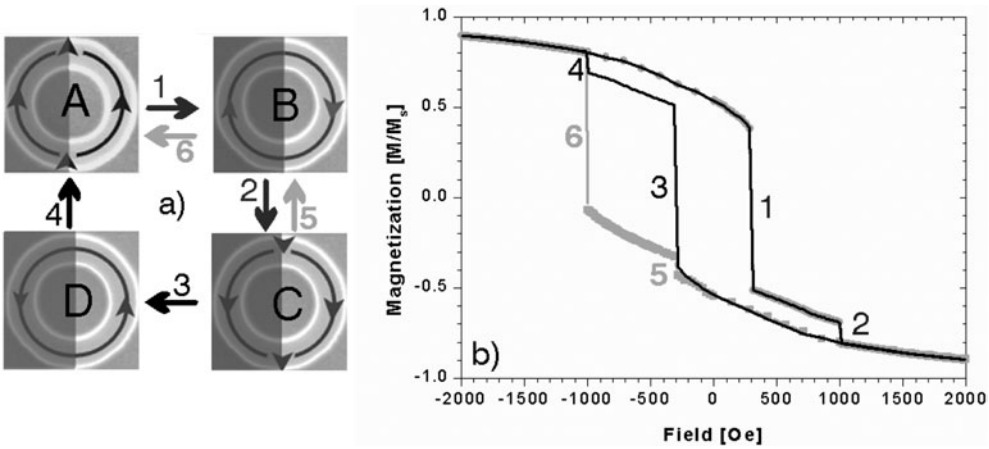

Figure 26. (a) Schematic diagrams of the possible magnetic configurations of rings. (b) Computed hysteresis loops for the magnetization of the bright right half of a ring (diameters: $d_{\text{ext}} = 1.8\ \mu$m, $d_{\text{int}} = 1\ \mu$m; thickness: 34 nm). Black: the loop of a ring reversing by switching into different vortex states. Grey: the loop of a ring reversing by switching always into the same vortex state.

state that follows the switch. From this we conclude that rings can be switched into both vortex states in a controlled and reproducible way.

5.2.3. Vortex circulation control. As shown earlier, the onion-to-vortex switching process is dependent on the pinning of the head-to-head domain walls due to edge roughness and other defects. In order to control the switching more precisely, notches can be introduced that act as artificial pinning sites. Micromagnetic simulations show not only that these

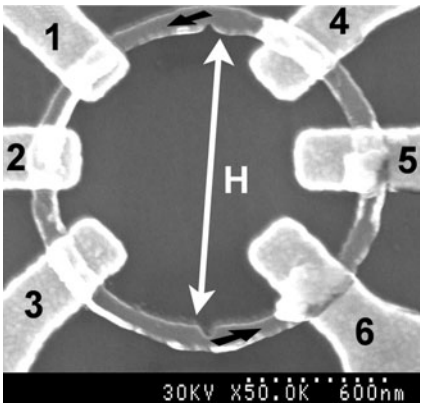

Figure 27. A scanning electron micrograph of a narrow permalloy ring (outer diameter 1.5 μm, inner diameter 1.3 μm). Clearly visible are the six non-magnetic electrical contacts and the two notches. The direction of the applied field H in the plane of the ring is indicated as well as the direction of the force that the domain walls feel after the applied field is reversed.

two possible vortex states (magnetization clockwise or anticlockwise) are attained during a complete hysteresis cycle but in addition that, by choosing the notch size and position as well as the direction of the applied field, the circulation direction of the vortex states can be selected [19] (section 5.2.2). This means that a particular vortex state can be induced using a uniform field to switch the rings from the appropriate onion state into the desired vortex state, as required for applications such as MRAM. As well as requiring controllable switching between states, such applications also demand the possibility of identifying (reading) the states using magnetoresistance measurements. Here we perform magnetoresistance measurements on rings with notches to directly confirm the possibility of controlling the magnetic switching using notches. The rings for these measurements were fabricated as explained in section 2.2.2. An SEM image is shown in figure 27. The MR measurements were done with a current of 10 μA using a standard lock-in technique in a dilution cryostat at 35 mK in order to minimize thermal noise. The field can be applied in any direction of the ring plane with a precision better than 0.1° by separately driving three orthogonal coils. The possibility of identifying with MR whether there is a domain wall between two contacts or not was exploited to determine the magnetic states and hence the switching processes during an hysteresis cycle of a ring. As discussed in detail in [13], the magnetoresistance is dominated by the familiar AMR. This means that the resistance has a maximum if all the magnetization is parallel (or antiparallel) to the current direction, which is the case if there is no domain wall between two contacts as then the magnetization and the current are parallel to the perimeter of the ring. If a domain wall is present between two contacts, the resistance is lowered, as inside the domain wall the magnetization is not parallel to the current any longer. The theoretical micromagnetic predictions for the switching properties were presented earlier in section 5 and [3]. Typical MR curves for two different pairs of contacts (full black triangles: 1–4; open black discs: 4–5) are shown in figure 28(a), while the current was injected between contacts 2 and 5 for all measurements. The general shape of such a curve can be described taking into account that at remanence the magnetization and the current are both parallel to the perimeter of the ring and hence the resistance is high. At saturation the magnetization is forced into a different direction leading to an angle between the current and the magnetization and hence to a decrease in the resistance. To explain the jumps in the MR curves, we look at the switching processes of a ring (onion-to-vortex transition at intermediate fields and vortex-to-opposite-onion transition

at high fields). It was suggested that the first switching process (onion to vortex at intermediate fields) is governed by the pinning of the domain walls [3]. As explained above, the pinning of the domain walls is achieved here by using notches of different sizes as seen in figure 27. The measurement was done using a field slightly misaligned with respect to the position of the notches (figure 27) so as to control the direction of the domain wall motion [19]. Starting with the field applied upwards (corresponding to a positive field), one expects that after relaxing the field, the ring attains the onion state with domain walls located at the notches between contacts 1 and 4, and between contacts 3 and 6 (inset (c) in figure 28(a)). As the field is reversed the domain walls feel a force in the direction indicated by the black arrows in figure 27. We set the direction of this force by choosing the angle between the field H and the position of the notches (shown in figure 27). As the notch between contacts 1 and 4 is smaller ($\approx 1/3$ of the ring width) than the one between 3 and 6 ($\approx 1/2$ of the ring width), the domain wall located between contacts 1 and 4 will depin first, move down and thereby reverse the left half of the ring, passing through contacts 1, 2, and 3. As it reaches the other domain wall still pinned between contacts 3 and 6, both walls annihilate and an anticlockwise vortex is created (inset (d) in figure 28(a)). Experimentally, this onion-to-vortex transition can be observed in the data from the two pairs of contacts (1–4 and 4–5) presented in figures 28(a) and (b), which show the field range of interest and show also data from a third pair of contacts (black stars: 1–2). Looking at the voltage measured between contacts 1 and 4 (full black triangles in figures 28(a) and (b)), one sees a sharp increase at -0.82 kOe showing that at this field the domain wall depins and leaves that part of the ring, indicating the onion-to-vortex transition. Looking at the voltage between contacts 1 and 2 (the lowest trace consisting of black stars in figure 28(b)), one sees a gradual decrease in the voltage with increasing reversed field as the spins are forced to rotate further and further towards the direction of the field and hence are less and less aligned with the direction of the current which lowers the resistance. At the switching field of the onion-to-vortex transition (-0.82 kOe) there is a clear jump indicating the reversal of the part of the ring between contacts 1 and 2, which is in agreement with the expected reversal of the left half of the ring during this transition. The second switching process is the transition from the vortex state (inset (d)) in figure 28(a) to the opposite onion state (inset (e)) in figure 28(a). In this switching process the right half of the ring reverses and opposite head-to-head walls are created again between contacts 1 and 4 and between 3 and 6. Experimentally this is observed as the voltage between contacts 1 and 4 (full black triangles in figures 28(a) and (b)) drops at -1.08 kOe showing that opposite head-to-head domain walls are created between these contacts. Furthermore, looking at the voltage measured between contacts 4 and 5 (open black discs) there is a clear jump at -1.08 kOe, indicating that the part of the ring between contacts 4 and 5 reverses at that field, which is in agreement with the anticipated reversal of the right half of the ring. As expected, it is also found that the area of the ring between contacts 2 and 3 reverses at the same field as the part of the ring between contacts 1 and 2 (-0.82 kOe) and the part between contacts 5 and 6 reverses at -1.08 kOe. From these results it can be concluded that using different sized notches, and choosing the direction of the field carefully, allows the controlled switching of the ring from the positive onion state pointing upwards into the anticlockwise vortex and from the reverse (negative) onion state pointing downwards into the clockwise vortex.

5.3. Additional switching processes

While the double-switching process described above occurs in the rings discussed so far, we have found different switching behaviours when the film thickness and ring width are varied over a wide range of values (film thickness for fcc Co between 5 and 34 nm, polycrystalline

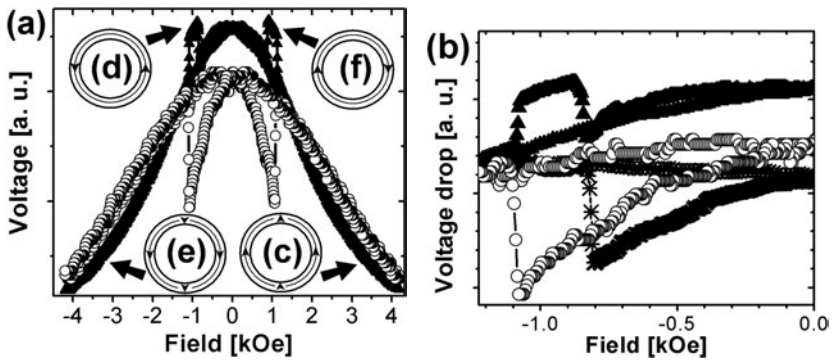

Figure 28. (a) Typical MR curves measured at different contacts with the current always flowing between contacts 2 and 5 (the data sets were shifted and scaled to arbitrary units to fit into one graph). The signal from contacts 1 and 4 (full black triangles) shows a clear two-step switching process with the voltage increasing when the ring is in the vortex state and no domain wall is present between contacts 1 and 4. The signal from contacts 4 and 5 (open black discs) shows a single reversal as the right side of the rings reverses. (b) A close-up for the interesting field range showing that the two switching processes in the signals of contacts 1 and 4 (full black triangles) coincide with the reversal of the magnetization of the part of the ring between contacts 1 and 2 (black stars) at −0.82 kOe and the reversal of the part between contacts 4 and 5 (open black discs) at −1.02 kOe.

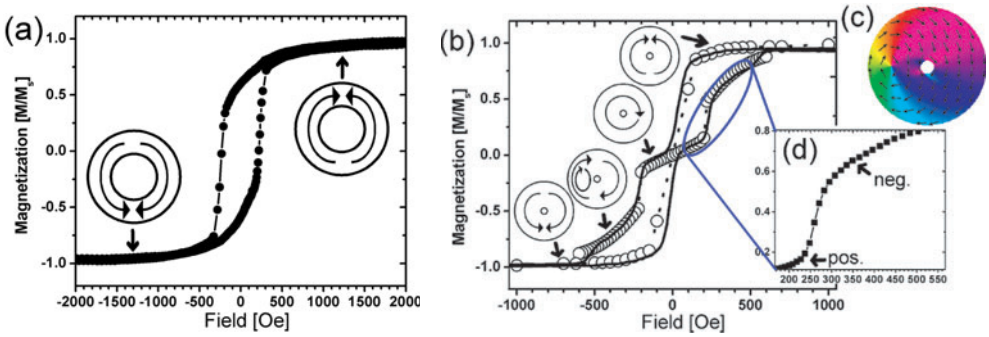

Figure 29. MOKE loops of an array of rings. (a) A hysteresis loop showing single switching in thin-film rings ($d_{ext} = 1700$ nm, $d_{int} = 1250$ nm, $t = 4$ nm; polycrystalline Co) with the magnetization configurations of the onion states shown schematically. (b) Triple switching in very wide rings with thick films ($d_{ext} = 1700$ nm, $d_{int} = 300$ nm, $t = 32$ nm; polycrystalline Co; experimental data: black line; micromagnetic simulation: empty circles). The magnetization configurations are shown schematically (from top to bottom: onion, vortex, 'vortexcore', and opposite onion states). (c) Micromagnetic simulation of the magnetization configuration in the 'vortexcore' state (the colour code is as in figure 16). (d) An enlargement of the experimental data in the interesting field region showing the difference in curvature when the field is applied to the ring in the vortex state (indicated with 'pos.') and in the 'vortexcore' state (indicated with 'neg.') confirming theoretical predictions [11].

Co between 2 and 34 nm, and polycrystalline permalloy between 2 and 45 nm; ring width between 5 and 90% of the outer diameter d_{ext}, with 90 nm $< d_{ext} <$ 2000 nm). d_{ext} is kept <2 μm for mesoscopic rings to prevent the occurrence of complicated and defect-dominated multi-domain states. In addition to the previously discussed double-switching process [3, 19], we find novel types of hysteresis behaviour: in very thin rings the reversal can occur with a single transition as seen in figure 29(a) and in thick and wide rings with triple switching as seen in figure 29(b). These additional switching processes are discussed in detail in [64].

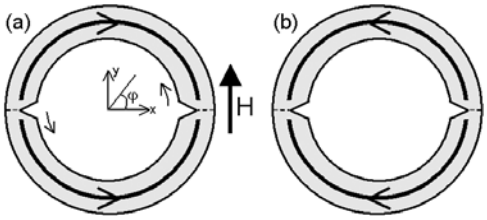

Figure 30. Schematic representations of the (a) right-onion and (b) left-onion states. The positions of the two domain walls are indicated by the dashed lines. The curved arrows indicate the direction of motion of the domain walls when the field is applied.

5.4. Onion-to-reverse-onion fast precessional switching

In this section we present a series of micromagnetic simulations that show how it is possible to achieve complete magnetization reversal in a fast and controllable manner without going through the intermediate vortex state. Rings of external diameter $d_{\text{ext}} = 250$ nm, internal diameter $d_{\text{int}} = 185$ nm, and thickness $t = 6$ nm have been considered. Typical Co parameters ($A = 3.0 \times 10^{-11}$ J m^{-1}, $M_s = 1.4 \times 10^6$ A m^{-1}) and damping $\lambda/\gamma = 0.02$ have been used. Magnetocrystalline anisotropy has been neglected. We have introduced two diametrically opposed notches at the inner edge of the ring in order to define equilibrium positions for the domain walls as shown in figure 30.

Starting from the right-onion state (figure 30(a)), stable at remanence after saturation along the $+x$-direction, our goal is to switch to the left-onion state (figure 30(b)) in a fast manner. A field applied along the $-x$-direction, opposite to the magnetization, would not exert any pressure on the walls due to the symmetry of the state. In a non-ideal case, a small pressure would appear due to defects or to some misalignment between the field and the walls. In any case, magnetization reversal would be inefficient, i.e. only a small component of the field exerts a pressure on the walls, and hard to control, because the depinning field would be very sensitive to defects and misalignments. Instead, the field pulse will be applied along the $+y$-axis, perpendicular to the magnetization, which will push the walls in the direction indicated by the curved arrows in figure 30(a).

Figure 31 shows the time evolution of the x- and y-average components of the magnetization when a square field pulse of height $H = 40$ mT $= 400$ Oe and width $\Delta t = 125$ ps is applied. Figure 32 shows the spin configuration at several instants during magnetization reversal. Starting from the right-onion state at $t = 0$ (figure 32(a)) there is an initial region in which m_x decreases very slowly, corresponding to a reversible deformation of the pinned walls (figure 32(b)). At approximately $t = 40$ ps the two walls depin from the notches and start moving around the ring (figure 32(c)). The Zeeman energy injected in the system is transferred to the walls leading to their motion, whose precessional nature can be seen in the high-frequency oscillations of m_y (figure 31). At $t = 125$ ps the field is removed, but the energy absorbed by the walls makes them continue the rotation around the ring (figures 32(d) and (e)). After rotating by 180° they reach the notches and become attached to them. Magnetization reversal is thus completed and the excess energy is dissipated through small wall oscillations (figure 31) around their equilibrium positions, a process known as 'ringing'. According to our calculations, the oscillations last another 1.5 ns, until all the energy is dissipated and equilibrium is reached. It should be pointed out that applying a second field pulse in the $-x$-direction after the first one is suppressed would increase the switching time and, most importantly, would eliminate ringing to a great extent. We do not address

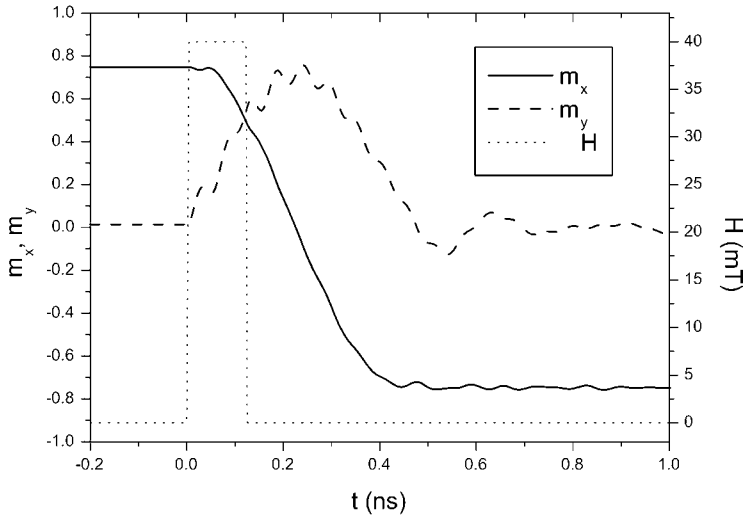

Figure 31. Time evolution of the average components of the normalized magnetization during reversal. The applied field is $H = 40$ mT (1 mT = 10 Oe) and the pulse width $\Delta t = 125$ ps.

this problem here because the purpose of this work is to demonstrate that, unlike in other approaches [1, 65], sub-nanosecond magnetization reversal can be achieved applying only one field pulse perpendicular to the magnetization.

In order to achieve fast and controllable switching it would be desirable if the domain walls moved at a constant velocity when rotating around the ring. However, they are continuously decelerated as they rotate for several reasons. First of all, the pressure P exerted by the applied field $\vec{H}$ on the walls, which is given by

$$P = \Delta\vec{M} \cdot \vec{H}, \tag{2}$$

where $\Delta\vec{M}$ is the difference between the magnetization vectors on either side of the wall, decreases as they move. Secondly, once the field is removed, no more Zeeman energy is injected into the system and the energy stored in the walls is dissipated progressively. Finally, the weak pinning due to surface roughness accelerates the energy dissipation and slows down the wall motion. Nevertheless, in figure 31 we observe a roughly constant slope in m_x during magnetization reversal, which seems to indicate that the walls are moving at a constant velocity. However, this picture can be misleading because, due to the curvature of the ring, m_x does not depend linearly on the wall velocity. In order to gain some insight into this problem we have considered a simplified model assuming that the walls are infinitely thin and that the magnetization vector is parallel to $\vec{u}_\varphi$, i.e. the unitary vector among the in-plane polar coordinate φ (figure 30(a)), everywhere. Therefore, the average magnetization $\langle\vec{m}\rangle$ in the onion state will be given by

$$\langle\vec{m}\rangle = V^{-1}\int_V \vec{m}\,\mathrm{d}v = \frac{1}{2\pi}\left[\int_{\varphi_1}^{\varphi_2}(-\vec{u}_\varphi)\,\mathrm{d}\varphi + \int_{\varphi_2}^{\varphi_1}\vec{u}_\varphi\,\mathrm{d}\varphi\right] = -\frac{1}{\pi}\int_{\varphi_1}^{\varphi_2}\vec{u}_\varphi\,\mathrm{d}\varphi, \tag{3}$$

where V is the ring volume and φ_1, φ_2 are the positions of the head-to-head and tail-to-tail walls, respectively (in figure 30(a) $\varphi_1 = 0$ and $\varphi_2 = \pi$, whereas in figure 30(b) $\varphi_1 = \pi$ and $\varphi_2 = 0$). Furthermore, if we assume that the two walls depin at the same time and that they move with the same constant angular velocity ω, then $\varphi_1 = \varphi_2 + \pi = \omega t$, and considering that

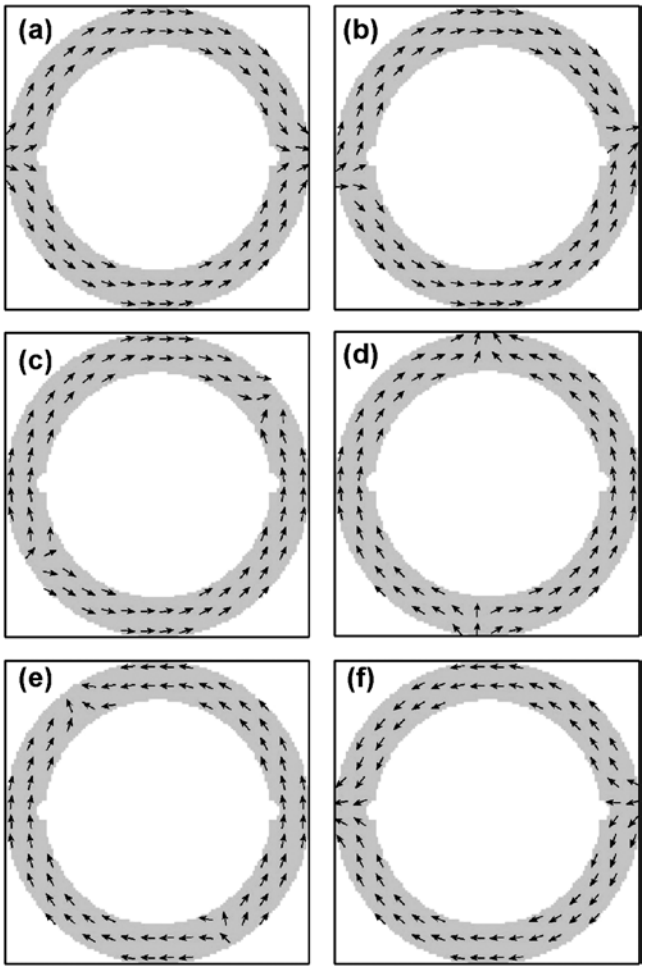

Figure 32. Magnetization configurations at $t =$ (a) 0 ps, (b) 50 ps, (c) 170 ps, (d) 250 ps, (e) 330 ps, and (f) 800 ps, corresponding to the reversal plotted in figure 31.

$\vec{u}_\varphi = -\sin(\varphi)\vec{u}_x + \cos(\varphi)\vec{u}_y$ we have

$$\langle \vec{m}(t) \rangle = \frac{2\alpha}{\pi}[\cos(\omega t)\vec{u}_x + \sin(\omega t)\vec{u}_y]. \tag{4}$$

We have introduced the parameter α to take into account the fact that the walls have a certain width and that the spins inside them are pointing mainly along the radial direction. Since it is observed that the internal structure of the walls remains roughly unchanged during reversal (figure 32), the shape of the curve should not be affected by this consideration and only a scaling factor is necessary. Figure 33 shows the time evolutions of $\langle m_x \rangle$ and $\langle m_y \rangle$ (solid curves) during magnetization reversal for a field pulse of height $H = 50$ mT and width $\Delta t = 125$ ps and the corresponding fitted curves (dashed curves) using equation (4). The fitting was done in the interval $t \in [54, 440]$ ps, approximately the time range during which the wall is not pinned at the notches and moves freely. The values $\alpha = 1.16$ and $\omega = 7.34 \times 10^9$ s^{-1} were obtained, the latter yielding a linear velocity $v = \omega r \simeq 7.34 \times 10^2$ m s^{-1}. It is observed that a good agreement is found in the net evolution of the magnetization (the high-frequency oscillations

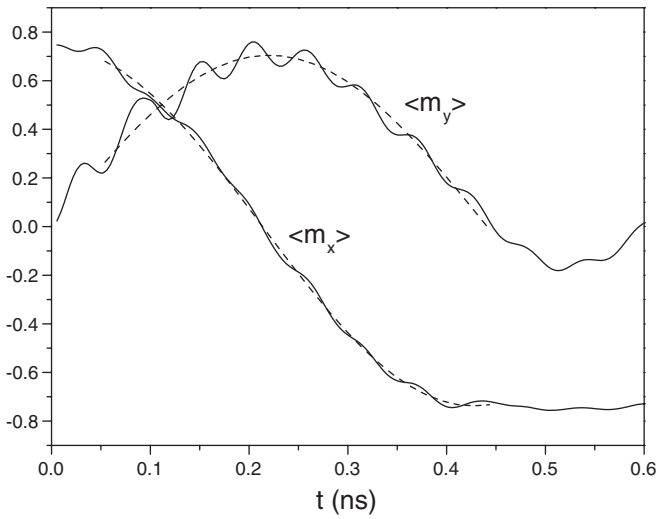

Figure 33. Fittings (dashed lines) of the time evolution of $\langle m_x \rangle$ and $\langle m_y \rangle$. The data (solid curves) correspond to the simulation plotted in figure 31 and they have been fitted to equation (4) in the time interval $t \in [54, 440]$ ps. The values $\alpha = 1.16$ and $\omega = 7.34 \times 10^9$ s^{-1} were obtained.

correspond to the precessional motion of the spins inside the walls and are not included in our model), indicating that the domain wall velocity is kept roughly constant during reversal. However, this is not always the case. Figure 34 shows the time evolution of the two in-plane components of the magnetization for different values of the applied field. It is observed that, as the field is lowered, the progressive deceleration of the walls becomes more apparent, i.e. the slope of the $\langle m_x \rangle$ curve decreases (figure 34(a)) and the $\langle m_y \rangle$ curve becomes more asymmetric (figure 34(b)). It should be noted, however, that in the initial part of the reversal, immediately after the walls depin from the notches, the velocities are only weakly dependent on the field, i.e. the average slopes are very similar to each other and only the amplitude of the oscillations changes. On the other hand, it is found that the depinning time slightly decreases with the applied field. Figure 35 shows the dependence of the depinning time t_{depin} with H, where t_{depin} is defined as the time at which $\langle m_x \rangle = 0.62$ (this particular value is chosen considering that at this point clearly the wall has already depinned and, at the same time, we are in the initial part of the curve, so the velocities are roughly independent of the applied field). The curve in figure 35 shows that t_{depin} cannot be lowered indefinitely by increasing H. On the contrary, there seems to be a minimum time for the transferring of a certain amount of Zeeman energy into the walls that allows them to depin from the notches and start moving. This minimum time is estimated to be roughly 40 ps. The Zeeman energy cannot be injected into the system at an arbitrarily high rate by applying larger fields than the ones considered here, because that would destroy the coherent structure of the onion state.

We have computed the magnetization reversal for several values of the field pulse height H and width Δt and the results are presented in figure 36, where the successful (open circles) and unsuccessful (black symbols) experiments have been marked. By a 'successful experiment' we mean one in which the final state is the left-onion state (figure 30(b)) and in which reversal proceeds similarly to the case described at the beginning of this section. In any other case, the experiment is considered unsuccessful. As can be seen, successful experiments can be achieved for a wide range of applied fields and pulse widths. The shape of the successful region suggests that the product $H\ \Delta t$ or, equivalently, the total Zeeman energy (assuming that

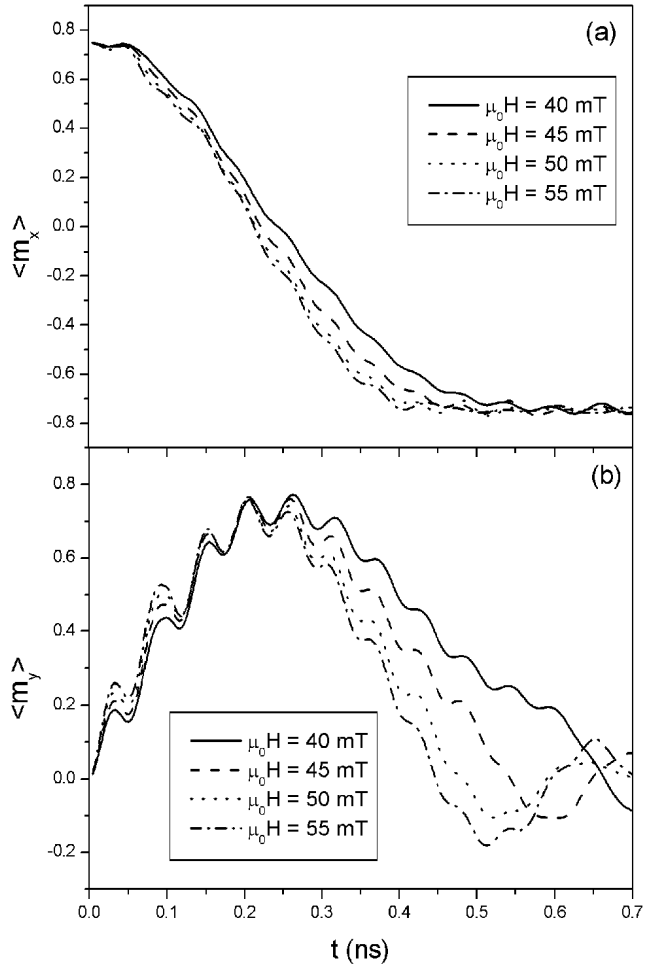

Figure 34. Time evolutions of (a) $\langle m_x \rangle$ and (b) $\langle m_y \rangle$ for different values of the applied field (1 mT = 10 Oe). The pulse width is $\Delta t = 125$ ps in all cases.

it is absorbed at a constant rate during the time interval Δt), should be kept within a certain range in order to reverse the magnetization successfully. To emphasize this we have plotted the curve $H\,\Delta t = 5 \times 10^{-12}$ T s, which crosses the successful region throughout its middle part. However, other factors need to be taken into account. First of all, obviously the applied field needs to be larger than the depinning field (23 mT approximately), which explains why no successful switching is obtained for $H = 20$ mT (black triangles). In the same manner, no depinning is achieved for $\Delta t = 25$ ps, indicating that, as discussed before, a minimum time of approximately 40 ps is required to transfer the Zeeman energy into domain wall motion. Secondly, for fields larger than 70 mT the structure of the onion state is destroyed. For the unsuccessful points on the lower left region of figure 36 (black squares) the walls are depinned, but the energy injected in the system is not enough to complete magnetization reversal and the walls stop before reaching the notches, pinned at regions where the artificial surface roughness is stronger. In contrast, in the upper right region (inverted triangles) the walls reach the notches with too much energy to remain pinned at them and they continue rotating around the ring until all the excess energy is dissipated. Finally, for $\Delta t > 200$ ps (black diamonds) the field

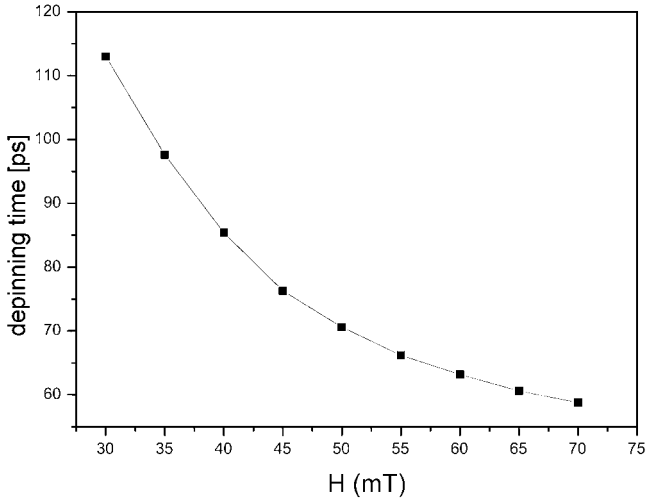

Figure 35. Depinning time as a function of the applied field. The depinning time t_{depin} is defined as the time at which $\langle m_x \rangle = 0.62$.

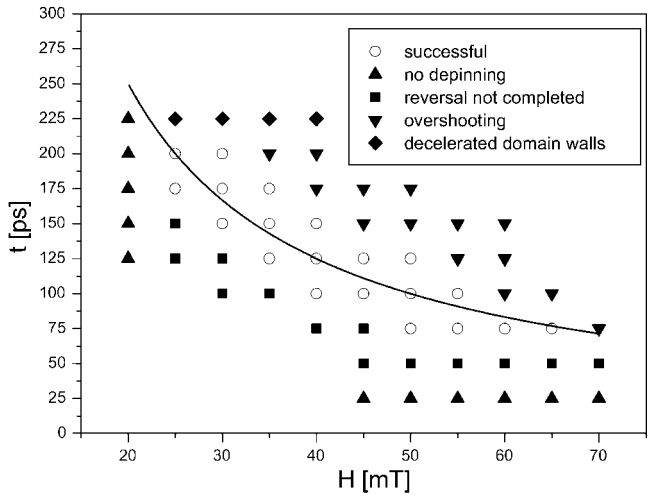

Figure 36. Diagram showing the successful (open circles) and unsuccessful (black symbols) experiments. The unsuccessful ones are labelled with different symbols according to the main feature of the reversal process.

is removed after the walls have rotated 45°, i.e. the point where m_y reaches its maximum value (figure 31). Once the walls have reached that point they are decelerated because there is a restoring force trying to align them with the field. Consequently, in this upper region the successfulness of the experiment becomes very critical with H and Δt.

6. Conclusions

We have reviewed current progress in the study of ferromagnetic ring structures, describing in detail our own recent work on the fabrication, magnetostatic configurations, and magnetodynamic switching of ferromagnetic rings. An important aspect of current research

is the development of appropriate fabrication processes, which allow the exploration of the geometry dependence of the magnetic properties. To this end we have developed the technique of prepatterned substrates to fabricate epitaxial fcc Co rings. While this ensures single-crystalline epitaxial magnetic layers, we find that the etching of the silicon can lead to additional edge roughness. Using a standard lift-off technique we can produce polycrystalline rings of various materials, some of which were contacted for MR measurements. We find that by optimizing the fabrication process, well defined rings down to the sub-100 nm regime can be made. We have briefly discussed the morphology and magnetism of the thin films used in this study, as knowledge of the inherent magnetic properties is a necessary prerequisite for understanding the influence of the geometry on the magnetic properties of the ring structures. In particular we relate the magnetic anisotropies to the crystalline structure of the materials used.

The magnetic states in rings fabricated using the different techniques have been extensively explored and a detailed picture is now beginning to emerge. We have shown that in rings there are two stable states at remanence: the flux-closure vortex state and the onion state characterized by two head-to-head domain walls. The nanoscopic spin structure of the head-to-head domain walls has been directly imaged and, depending on the geometrical parameters, either transverse or vortex walls are found. These findings are crucial in providing direct proof of the existence of the different types of head-to-head domain wall, which characterize the magnetic states. This is an illustration of the competition between the stray field (magnetostatic) and exchange interaction, the former becoming more important as the width of the ring is reduced. Comparing epitaxial and polycrystalline rings it can be seen that the magnetocrystalline anisotropy is only important for wide rings, whereas for narrow rings the shape is the driving force dominating the magnetization configurations. In the limit of the disc, the dominant energy term is the magnetostatic energy, but when a magnetocrystalline cubic anisotropy is present, the disc accommodates for this term by exhibiting a quadrant domain structure. We find that the width of the domain walls between domains increases with the distance from the vortex core in good agreement with micromagnetic simulations.

Having understood the equilibrium states that rings attain, we are able to better explain the switching processes between the magnetic states, in particular the nucleation-free domain wall propagation governing the onion-to-vortex transition. We show that the presence of imperfections is necessary to explain this switching behaviour. Furthermore, comparison of epitaxial and polycrystalline rings shows that polycrystalline rings have a smaller switching field distribution, which might be attributed to a more regular spread of a large number of imperfections (grain boundaries) as compared to the epitaxial single-crystalline films. Thus for applications, polycrystalline rings might be well suited. What is more, using notches as artificial pinning sites allows control of the onion-to-vortex transition and for selection of a desired circulation direction of the vortex state. Furthermore, a precessional transition from the onion state to the reverse onion state is investigated using micromagnetic simulations. By applying only a field pulse perpendicular to the net magnetization a fast reversal (approximately 400 ps), which is well characterized (depinning and propagation of domain walls, no nucleation involved), robust (it can be achieved for a wide distribution of applied fields and pulse widths), controllable (if the appropriate amount of energy is injected at the appropriate rate the domain wall velocity is approximately constant during reversal), can be achieved.

In conclusion, while many of the simple micromagnetic predictions have been observed, the experiments have revealed unexpected subtleties in the magnetic behaviour, which in turn can be used to refine the modelling and improve our understanding of ring magnets. While the ring shape has a very high degree of symmetry, it shows nonetheless a range of intriguing properties, which are only just beginning to be understood.

Acknowledgments

The work presented in this article would not have been possible without the support of a number of people and institutions. The authors would like to thank Z Cui for developing the technique of prepatterned substrates, L J Heyderman for the patterning of lift-off rings, and G Faini and E Cambril for the fabrication of rings with non-magnetic contacts. We would like to thank J Rothman, who started the ring project in Cambridge, Y G Yoo for some of the MOKE measurements, A Bleloch for STEM imaging, R Speaks for helping with FIB, T L Monchesky and J Unguris for SEMPA imaging, E Bauer and the SPELEEM group at the ELETTRA synchrotron for PEEM imaging, and W Wernsdorfer for help with MR measurements. This work was supported by the EU ESPRIT network MASSDOTS, the Gottlieb Daimler and Carl Benz Foundation (MK), the Portuguese PRAXIS XXI programme (CAFV), and the European Commission (LL-D., EC HPMF-1999-00141).

References

[1] Zhu J-G, Zheng Y and Prinz G A 2000 *J. Appl. Phys.* **87** 6668
[2] Miller M M, Prinz G A, Cheng S-F and Bounnak S 2002 *Appl. Phys. Lett.* **81** 2211
[3] Rothman J, Kläui M, Lopez-Diaz L, Vaz C A F, Bleloch A, Bland J A C, Cui Z and Speaks R 2001 *Phys. Rev. Lett.* **86** 1098
[4] Zheng Y and Zhu J-G 1997 *J. Appl. Phys.* **81** 5471
[5] Cowburn R P, Koltsov D K, Adeyeye A O, Welland M E and Tricker D M 1999 *Phys. Rev. Lett.* **83** 1042
[6] Gubbiotti G, Albani L, De Carlotti G, Di Crescenzi M, Fabrizio E, Gerardino A, Donzelli O, Nizzoli F, Koo H and Gomez R D 2000 *J. Appl. Phys.* **87** 5633
[7] Pokhil T, Song D and Nowak J 2000 *J. Appl. Phys.* **87** 6319
[8] Fruchart O, Nozières J P, Wernsdorfer W, Givord D, Rousseaux F and Decanini D O 1999 *Phys. Rev. Lett.* **82** 1305
[9] Yu J, Ruediger U, Thomas L, Parkin S S P and Kent A D 1999 *J. Appl. Phys.* **85** 5501
[10] Stoner E C and Wohlfarth E P 1948 *Phil. Trans. R. Soc.* A **240** 599
[11] Lopez-Diaz L, Rothman J, Kläui M and Bland J A C 2000 *IEEE Trans. Magn.* **36** 3155
[12] Bland J A C, Kläui M, Lopez-Diaz L and Rothman J 2000 *Patent Specification* SAH01427
[13] Kläui M, Vaz C A F, Bland J A C, Wernsdorfer W, Faini G and Cambril E 2002 *Appl. Phys. Lett.* **81** 108
[14] Kläui M, Vaz C A F, Rothman J, Bland J A C, Wernsdorfer W, Faini G and Cambril E 2003 *Phys. Rev. Lett.* **90** 97202
[15] Kasai S, Niiyama T, Saitoh E and Miyajima H 2002 *Appl. Phys. Lett.* **81** 316
[16] Hirohata A, Yao C C, Leung H T, Xu Y B, Guertler C M and Bland J A C 2000 *IEEE Trans. Magn.* **36** 3068
[17] Welp U, Metlushko V, Vlasko-Vlasov V K, Crabtree G W, Hiller J, Zaluzec N J and Ilic B 2002 *47th Annu. Conf. on Magnetism and Magnetic Materials (Tampa, FL, 2002)* Number CC-12
[18] Vavassori P, Grimsditch M, Novosad V, Metlushko V, Ilic B, Neuzil P and Kumar R 2002 *47th Annu. Conf. on Magnetism and Magnetic Materials (Tampa, FL, 2002)* Number FC-07
[19] Kläui M, Rothman J, Lopez-Diaz L, Vaz C A F, Bland J A C and Cui Z 2001 *Appl. Phys. Lett.* **78** 3268
[20] Heyderman L J, Kläui M, Rothman J, Vaz C A F and Bland J A C 2003 *J. Appl. Phys.* at press
[21] Chen W and Ahmed H 1993 *Appl. Phys. Lett.* **62** 13
[22] Cui Z, Gerardino A, Gentili M, Di Fabrizio E and Prewett P D 1998 *J. Vac. Sci. Technol.* B **16** 3284
[23] Larmer F and Schilp A 1999 *Patent Specifications* DE4241045, US5501893, EP625285
[24] Kläui M M 2000 Nanomagnetism of prepatterned epitaxial structures *Master's Thesis* University of Cambridge
[25] Kleiber M, Kümmerlen F, Löhndorf M, Wadas A, Weiss D and Wiesendanger R 1998 *Phys. Rev.* B **58** 5563
[26] Lebib A, Li S P, Natali M and Chen Y 2001 *J. Appl. Phys.* **89** 3892
[27] David C and Hambach D 1999 *Microelectron. Eng.* **46** 219
[28] Chen Y, Lebib A, Li S P, Natali M, Peyrade D and Cambril E 2001 *Microelectron. Eng.* **57** 405
[29] Li S P, Peyrade D, Natali M, Lebib A, Chen Y, Ebels U, Buda L D and Ounadjela K 2001 *Phys. Rev. Lett.* **86** 1102
[30] Iyer S S, Arienzo M and de Frésart E 1990 *Appl. Phys. Lett.* **57** 893
[31] Hanbücken M, Métois J J, Mathiez P and Salvan F 1985 *Surf. Sci.* **162** 622
[32] Park H, Ko D, Apte P, Helms C R and Saraswat K C 1998 *Electrochem. Solid-State Lett.* **1** 77

[33] Hashim I, Joo H S and Atwater H A 1995 *Surf. Rev. Lett.* **2** 427
[34] Hashim I and Atwater H A 1994 *J. Appl. Phys.* **75** 6516
[35] Pearson W B 1967 *Lattice Spacings and Structures of Metals and Alloys* vol 2 (Oxford: Pergamon)
[36] Vaz C A F and Bland J A C 2000 *Phys. Rev.* B **61** 3098
[37] Vaz C A F and Bland J A C 2001 *J. Appl. Phys.* **89** 7473
[38] Heckmann O, Magman H, le Fevre P, Chandesris D and Rehr J J 1994 *Surf. Sci.* **312** 62
[39] Cerdá J R, de Andres P L, Cebollada A, Miranda R, Navas E, Schuster P, Schneider C M and Kirschner J 1993 *J. Phys.: Condens. Matter* **5** 2055
[40] Kowalewski M, Schneider C M and Heinrich B 1993 *Phys. Rev.* B **47** 8748
[41] Heinrich B and Cochran J F 1993 *Adv. Phys.* **42** 523
[42] Hillebrands B, Fassbender J, Junglblut R, Güntherodt G, Roberts D J and Gehring G A 1996 *Phys. Rev.* B **53** R10548
[43] Fujiwara H, Kadomatsu H and Tokunaga T 1983 *J. Magn. Magn. Mater.* **31–34** 809
[44] http://math.nist.gov/oommf
[45] Li S P, Lew W S, Bland J A C, Natali M, Lebib A and Chen Y 2002 *J. Appl. Phys.* **92** 7397
[46] Bekaert J, Buntinx D, Van Haesendonck C, Moshchalkov V V, De Boeck J, Borghs G and Metlushko V 2002 *Appl. Phys. Lett.* **81** 3413
[47] Castano F J, Ross C A, Frandsen C, Eilez A, Gil D, Smith H I, Redjdal M and Humphrey F (unpublished)
[48] Zhu X, Grütter P, Metlushko V and Ilic B (unpublished)
[49] Locatelli A, Cherifi K S, Heun S, Marsi M, Ono K, Pavlovska A and Bauer E 2002 *Surf. Rev. Lett.* **9** 171
[50] Scheinfein M R, Unguris J, Kelley M H, Pierce D T and Celotta R J 1990 *Rev. Sci. Instrum.* **61** 2501
[51] McMichael R D and Donahue M J 1997 *IEEE Trans. Magn.* **33** 4167
[52] Lopez-Diaz L, Kläui M, Rothman J and Bland J A C 2001 *Physica* B **306** 211
[53] Vaz C A F, Lopez-Diaz L, Kläui M, Bland J A C, Monchesky T L, Unguris J and Cui Z *Phys. Rev.* B **67** 140405 (R)
[54] Bruno P 1999 *Phys. Rev. Lett.* **83** 2425
[55] Yamamoto K, Matsuyama H, Hamakawa Y and Kitada M 1994 *J. Appl. Phys.* **75** 2998
[56] Guo Y and Zhu J-G 1994 *J. Appl. Phys.* **75** 6388
[57] Mattheis R, Ramstöck K and McCord J 1997 *IEEE Trans. Magn.* **33** 3993
[58] Hubert A and Rave W 1999 *J. Magn. Magn. Mater.* **196/197** 325
[59] Sinnecker E H C P, Guimarães A, Kläui M, Vaz C A F, Bland J A C and Heyderman L J 2003 *Int. Conf. on Magnetism (Rome, Italy, 2003)*
[60] Kläui M, Lopez-Diaz L, Rothman J, Vaz C A F, Bland J A C and Cui Z 2002 *J. Magn. Magn. Mater.* **240** 7
[61] Yoo Y G, Kläui M, Vaz C A F, Bland J A C and Heyderman L J 2003 *Appl. Phys. Lett.* **82** 2470
[62] Lopez-Diaz L, Rothman J, Kläui M and Bland J A C 2001 *J. Appl. Phys.* **89** 7579
[63] Clegg W W, Heyes N A E, Hill E W and Wright C D 1991 *J. Magn. Magn. Mater.* **95** 49
[64] Kläui M, Vaz C A F and Bland J A C 2003 unpublished
[65] Anguelouch A, Schrag B D, Xiao G, Lu Y, Trouilloud P L, Wanner R A, Gallagher W J and Parkin S S P 2000 *Appl. Phys. Lett.* **76** 622